TU Delft

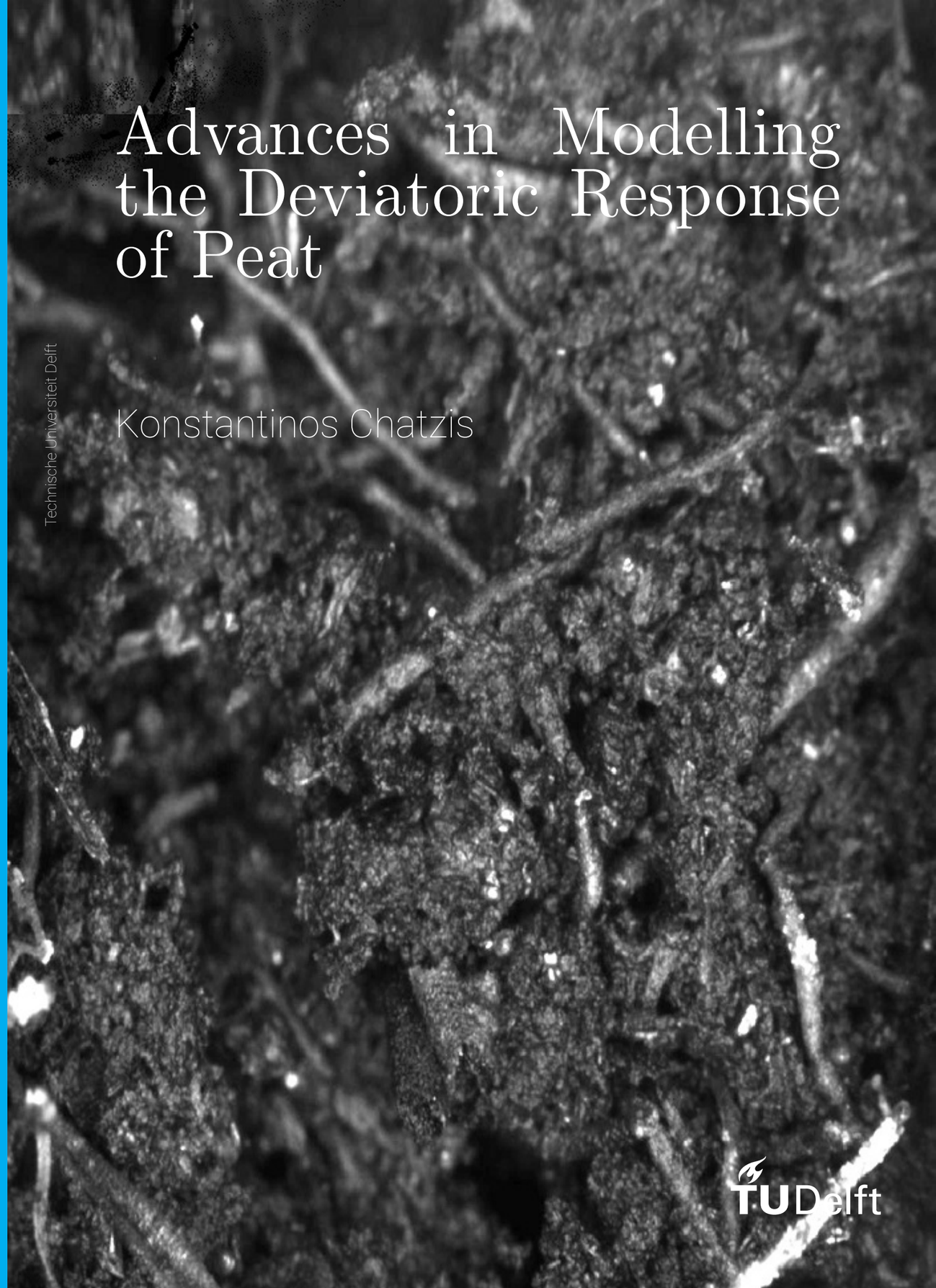
Advances in Modelling the Deviatoric Response of Peat
Konstantinos Chatzis
Technische Universiteit Delft
TU Delft

Advances in Modelling the Deviatoric Response of Peat

by

Konstantinos Chatzis

to obtain the degree of Master of Science
at the Delft University of Technology,
to be defended publicly on Wednesday December 12, 2018 at 01:30 PM.

Student number:	4627822	
Project duration:	February 20, 2018 – December 12, 2018	
Thesis committee:	Prof. dr. ir. C. Jommi,	TU Delft, supervisor (chair)
	Dr. ir. A. C. Dieudonné,	TU Delft
	Dr. X. Liu,	TU Delft
	Ir. S. Muraro,	TU Delft, daily supervisor

The image on front page is adopted by Jommi et al. (2018).

An electronic version of this thesis is available at `http://repository.tudelft.nl/`.

TU Delft

Preface

This Thesis marks the end of my studies at TU Delft as a student of the Master Geo-engineering. I can say that my studies at TU Delft were full of challenges and offered me the possibility to study on a topic that I am really interested in. In these two and a half years I had the chance to meet and collaborate with several people, who helped me to accomplish my goals, and I would like to thank them.

First of all, I would like to express my appreciation to my thesis supervisor Prof. Dr. Cristina Jommi. It was a pleasure to have her as a supervisor. Her guidance and valuable advice widened my horizons related to the science of geotechnical engineering, while also motivated me to continue my Thesis.

Second, I would like to thank Dr. A. C. Dieudonné for her contribution on this Thesis. My dissertation would have never been accomplished without her help on the use of FEM software LAGAMINE and on the programming of the proposed model.

I would like to thank also Dr. X. Liu for his participation at this interesting topic.

In addition, I could not forget to express my special gratitude to my daily supervisor Stefano Muraro. He was always available at helping me and guiding me, with great input and advice. I could not have reached to such an end result without him.

Last but not least, my special thanks to my friends, Eleni, Vassilis, Giorgos, Nikiforos, Dimitris and many others. I would like to thank my family for supporting me all these years. With their guidance and trust in me, I was able to follow my dreams.

Konstantinos Chatzis
Delft, December 2018

Abstract

The term peat is commonly used to describe organic soils, composed of fragmented plant remains and fibers. Despite the extensive research on the behaviour of peat during the last 50 years, the vast majority of the attention was devoted to the volumetric behaviour. Only few attempts are reported to model the deviatoric behavior of peat, which is fundamental in many geotechnical applications as dykes founded on peat layers. This Thesis represents an attempt to understand the current knowledge on the deviatoric behaviour of peat with the aid of an hierarchical simple elasto-plastic model.

The constitutive model was conceptually developed aiming for the use of a limited number of parameters with an easy way of determination. This choice aligns with the needs of engineering practice, which demands the use of models with few and comprehensive parameters. The constitutive ingredients of the model have been derived from direct experimental evidences. The model requires 10 parameters, 5 out of them are the classical parameters of the well-known Modified Cam-clay model.

The high compressibility of the peat along with its high friction angle intensify the end restraints occurring due to the platens of triaxial apparatus. In order to account for the effects of the boundaries, the constitutive model has been implemented in the Finite Element Programme LAGAMINE and the tests have been simulated as Boundary Value Problems. The model is in qualitative agreement with the experimental data and, in particular, with quantitative agreement until 20% of strain for the case of consolidated drained triaxial tests. To be able to reproduce properly the case of consolidated undrained triaxial tests which impose an isochoric response, one parameter associated with the flow rule of the model should be changed. This change of a parameter is related to the fact that the fibers in the peat specimen are not considered explicitly in the constitutive equations, although they can alter the deformational response of peat under some kinematic constraints and influence the mechanical response in a predominant way at high strain levels.

Overall, the constitutive model developed in this Thesis gives good quantitative results until 20% of axial strain. Further research on the influence of fibers on the response of peat under different strain paths and on the consequent matrix-fiber interaction should be done in order to have a model with predictive capabilities until high strain levels.

Contents

List of Figures

List of Tables

Chapter 1

Introduction

1.1 Problem Statement

The subsurface of the Netherlands is extensively composed of peat and organic soils, ensuing a plethora of construction challenges to be dealt. The problems arising from the presence of peat can be attributed to two parts of the behavior of peat, the volumetric and the deviatoric.

From experimental point of view, several researchers have studied the shear behavior of fibrous peat, composed of fragmented plant remains fossilized under water and pressure (Radforth, 1969; van der Heijden et al., 1994), and concluded that the peat strength is of frictional nature with small cohesion intercepts mainly due to fibers entanglements rather than cohesive bonds (Landva and La Rochelle, 1983; Yamaguchi et al., 1985). Mesri and Ajlouni (2007) state that fibrous peat presents exceptionally high frictional resistance as it can be seen in the Table 1.1 (Mesri and Ajlouni, 2007). More specifically, Yamaguchi et al. (1985) determined from triaxial tests, that the friction angle varies from 35 to 55 depending on the orientation of principal stresses with respect to the predominant (horizontal) orientation of fibers. Farrell et al. (1999) showed lower values of frictional angle obtained from direct shear and ring shear tests. The difference between the values of ϕ' obtained by the triaxial and direct/ring shear tests can be attributed to the fact that the latter tests estimate the frictional resistance of the matrix without the reinforcing effect of fibers which are activated during a triaxial test. However, several doubts still remain.

Previous research on the geotechnical response of peat has mainly focused on the volumetric behaviour from a constitutive viewpoint. Only few attempts to model the deviatoric behaviour of peat are reported. Yamaguchi et al. (1985) firstly attempted to model the deviatoric behavior of peat, based on the Modified Cam clay (Roscoe and Burland, 1968) coupled with an experimentally based stress-dilatancy law. Following attempts include the application of the Soft Soil Creep model and its anisotropic version (den Haan and Feddema, 2013; den Haan, 2014) and the elastic-plastic model by Li and Dafalias (2000) (Yang et al., 2016). Despite the capability of these attempts to capture the ultimate state of peat detected in the laboratory tests, their major limitation was the significant overestimation of the stiffness in the deviatoric stress-strain response. This cannot be neglected, as in geotechnical designs where peats are encountered, the serviceability limits rule the design criteria. These considerations call for an adequate geotechnical description of the pre-failure response of peat.

Table 1.1: Friction Angle of Fibrous Peats from Triaxial Compression Tests on Vertical Specimens (Mesri and Ajlouni, 2007)

Source	Peat	w_o (%)	ϕ' (degrees)
Adams (1961)	Muskeg	375–430	50–60
Adams (1965)	Moose River	330–600	48
Ozden et al. (1970)	Muskeg	800	46
Tsushima et al. (1977)	Muck	—	52–60
Yasuhara and Takenaka (1977)	Omono	—	50–60
Tsushima et al. (1982)	Muck	—	51
Edil and Dhowian (1981) and Edil and Wang (2000)	Middleton	500–600	57
	Portage	600	54
Landva and LaRochelle (1983)	Escuminac	1,240–1,380	40–50
Marachi et al. (1983)	San Joaquin	200–500	44
Yamaguchi et al. (1985a,c,d)	Ohmiya	960–1,190	51–55
	Urawa	980–1,260	53
Ajlouni (2000)	Middleton	510–850	60

The vast majority of the previous models for the deviatoric behaviour of peat have been calibrated and tested based on experimental results coming from undrained triaxial compression tests. However, triaxial tests pose severe limitations to the direct determination of the main constitutive ingredients. An essential assumption when considering triaxial tests is the uniformity of deformation of the specimen, as every representative information (volumetric changes and axial displacement are used to calculate radial and axial stresses respectively) about the true material behavior obtained from the test arises from this convention. Apart from the insufficient drainage, membrane effect and self-weight which constitute causes of non-uniform deformation of a triaxial specimen, the most crucial cause of this non-uniformity is the end restraint (Sheng et al., 1997).

End restraint is the formation of dead zones at the ends of the sample caused be the radial friction forces coming from the end platens of the triaxial specimens. Consequently, shear stresses develop at the cap and base forming dead zones which provide an additional confinement to the specimen. In addition, barreling effect and concentration of dilation in local zones are caused, not allowing to obtain information for the true material behavior. To overcome this limitation, Taylor (1941) has proposed length to diameter ratio of 2 to 1 or the use of frictionless ends in length to diameter ratio of 1 to 1. The former ratio has been proposed by other researchers too after having executed a large number of experiments in sands and clays (Shockley and Ahlvin, 1960; Rowe and Barden, 1964). It has to be explained that the use of frictionless ends is difficult to be applied in real laboratory conditions, but it is the only way to achieve a uniform deformation and a plastic zone failure (Lade and Tsai, 1985), so as to obtain representative shear strength parameters.

It seems that the problem of end restraints has been thoroughly investigated, but for the case of peat the use of widely adopted ratios is rather questionable as the compressibility of peat is 5 to 20 times the compressibility of soft clay in the same range of pressures (Mesri and Ajlouni, 2007). This can be explained by looking into Figure 1.1, where the comparison in the failure mode

between a typical clay and peat specimen with friction ends is depicted. It is clearly observed that the peat specimen is subjected to a larger deformation and the portion of the sample not affected by the dead zone is significantly smaller than for the case of clay sample. This problem arises the concern of possible misinterpretation of triaxial tests on peat with possible severe mistakes in shear strength and stiffness parameters obtained from the tests which cannot be neglected as in the case of sand or clay (Bishop and Green, 1965). From a modelling viewpoint, each experimental test should then be treated as a boundary value problem.

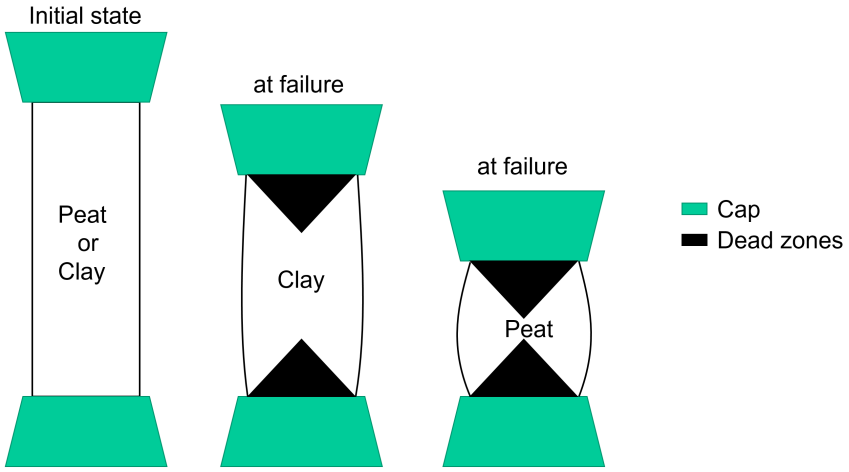

Figure 1.1: Deformation of clay and peat specimen with the use of friction ends

In the engineering practice, where the safety assessment of existing dykes or the design of new embankments is necessary, the development of a reliable constitutive model is essential. Constitutive models for soils are usually based on experimental behavior observed in laboratory tests. It is therefore important that such tests are performed unbiased and the recorded data truly represent the stress-strain behavior of the soil. This can be achieved only by applying adequately uniform conditions in triaxial tests. However, the boundary conditions imposed to the sample with standard laboratory devices may be far from uniform.

1.2 Research Questions

The main objective of this master Thesis is *to advance the current modelling approach for the deviatoric behaviour of peat by proposing a simple constitutive model with a limited amount of parameters in the framework of elasto-plasticity.*

The purpose of this Thesis is to attempt to reproduce the deviatoric behavior of the peat by numerical means with a simple and straightforward model. The well-established Modified Cam clay model Roscoe and Burland (1968) seems adequate to offer this possibility without developing advanced notions of constitutive modelling. In addition, the previous aforementioned modelling attempts was based mainly on the MCc framework indicating that this path is possible.

In Figure 1.2 the prediction of the MCc model in terms of stress path, deviatoric stress-strain and excess pore water pressure development is depicted in comparison with the corresponding experimental curves. It is observed that the MCc fails to reproduce the response of peat as it clearly overestimates the stiffness in the deviatoric stress-strain response (1.2c) and the rate of the excess pore pressure (1.2b). Finally, the stress path of Normally Consolidated clay, predicted by the MCc model is not representative for a material like peat.

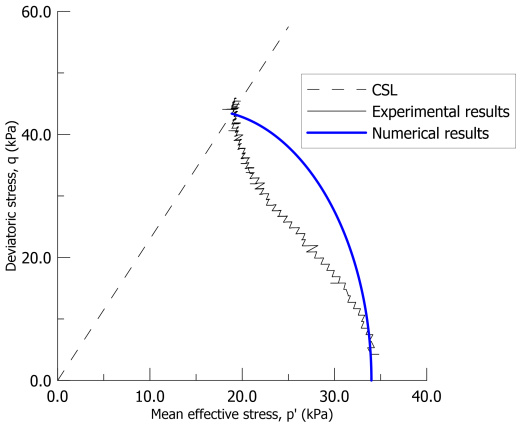

(a) Effective stress path

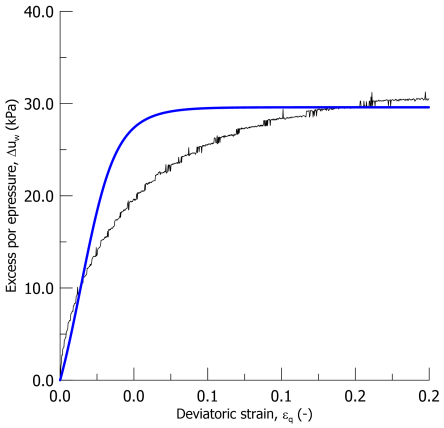

(b) Excess pore pressure vs deviatoric strain

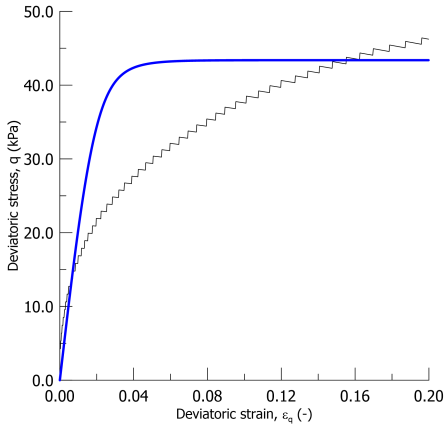

(c) Deviatoric stress-strain

Figure 1.2: Response of peat in laboratory and MCc prediction

The drawbacks of the MCc model outlined above indicate that the main ingredients of this model should be adopted in order to deal with the response of the peat. Hence, the research questions can be organized to the basic ingredients of plasticity, as the development of a new constitutive model based on the Cam clay framework is dictated by these ingredients. So, the proposed research questions are here formulated:

Is associated plasticity suitable for describing the pre-failure behavior of peat specimens affected by end restraints? Which method of measuring global stresses and strains is more suitable for describing the pre-failure stress-strain response of peat?

The impact of flow rule is not only important at failure in soils, which has been shown numerically by Gens and Potts (1988) and Lagioia and Panteghini (2014), among others, but is also significant at reproducing the pre-failure response. It is well known that the MCc suffers from the overestimation of K_0 values (Gens, 1982; Alonso et al., 1990), meaning that the shear strains are over-predicted. Thus, various approaches to tackle this issue has been proposed.

In addition, Sheng et al. (1997) demonstrated that the effects of non-uniformities on the analysis of stress-strain and strength properties of the soil also depend on how the global stresses and strains are computed from triaxial tests data.

Why the yield surface introduced by the Modified Cam clay model (Roscoe and Burland, 1968) is inappropriate to describe the peat behavior and how the formulation of the yield surface should be modified in order to have satisfying results?

The majority of the constitutive models have been developed to investigate the behavior of materials, like sands and clays. The MCc model has been developed to examine primarily the mechanical response of the clay of Cam river. Hence, it is reasonable to consider that this type of yield loci (Modified Cam clay) cannot represent the yield surface of the examined peat.

Is the hardening law used in the majority of constitutive models based on Cam clay theory appropriate for capturing the stress strain behavior of peat? If not, how can this be tackled?

Classical critical state models traditionally assume that the expansion of the yield locus (i.e. hardening of the soil) is controlled merely by the plastic volumetric strain. Indirect information on the hardening of peats can be found from undrained compression triaxial tests, where a "hook" is exhibited. This "hook" can be comparable to the undrained behavior of sands, where a mixed hardening law has been employed (Nova and Wood, 1979).

How the model performs if the experiments are treated numerically as a Boundary Value Problem?

Due to the intense end restraint formation in peat specimens, single element tests are not adequate to model triaxial tests of peat. Hence, the experiments should be modelled as a Boundary Value Problem.

1.3 Methodology

The work of this Thesis is based on laboratory tests conducted by Muraro (2018). Consolidated Undrained triaxial Test (TxCU) and Consolidated Drained Triaxial Test (TxCD) on reconstituted peat samples were conducted both with rough and smooth end platens. These laboratory results constitute the base on which the data from numerical analyses will be compared.

To answer the research questions, the work must be subdivided into several domains:

- The triaxial compression test is a boundary value problem which can be simulated by a finite element (FEM) program. In this master Thesis, Lagamine is the preferred FEM program. An appropriate mesh should be constructed where the platens of triaxial specimen are modelled either as rough or smooth to investigate the effect of end restraints. The reason for modelling only the platens as rough or smooth initially lies to the fact that diameter of peat triaxial specimens during the tests is not altered during the shearing and remains in full contact with the platens.

- The laboratory tests are also simulated using the Modified Cam clay model (MCc) which can incorporate either an associative flow rule (classical Modified Cam clay) or a non-associated flow rule. Herein, it is attempted to understand at what degree the MCc captures the pre-failure behavior of peat.

- Having found the limitations of MCc, single element tests are performed through a pre-existing constitutive driver to investigate the effect of the other constitutive ingredients on the response of peat. The goal of theses analyses is to investigate the influence of the inclusion of a mixed hardening law in a critical state model like MCc.

- However, the triaxial tests cannot be modelled adequately by a single element test as they constitute a boundary value problem and multiple elements are demanded in order to be modelled sufficiently. The model with the modified constitutive ingredients is implemented

into the Finite Element software LAGAMINE and the corresponding analyses to the laboratory tests are executed.

1.4 Limitations

This research project comprises an extensive literature study regarding peat response in triaxial compression and different constitutive models. Furthermore, numerical analyses are executed in order to compare different constitutive ingredients and to establish a basis on which a constitutive model can be developed. This model is desired to capture the peat behavior in triaxial compression tests.

Although the peat specimens in the laboratory are subjected to creep deformations, the models used in the numerical analyses do not deal with time dependent behavior. All the tests have been performed with the same strain rate in order not to induce different creep effects in the tests. Hence, the study of creep is out of the scope of this Thesis.

Moreover, the peat is assumed to contain a certain amount of gas bubbles due to the biogenic degradation of the organic matter, which are expelled during the triaxial compression. The influence of gas bubbles in the hydro-mechanical response of the material is not examined in this Thesis.

In addition, the isotropic consolidation on which they specimens were subjected prior to the shear stage, which contributes to the response of the peat to a certain extent, was not modelled in this Thesis.

Finally, all Finite Element models investigated are axisymmetric (2D). Despite the three-dimensional (3D) type of triaxial compression, the computational gains of 2D axisymmetric analysis render the implementation of 3D numerical model unprofitable.

1.5 Thesis outline

With regards to the above considerations, the Thesis is organized in six chapters in total.

Chapter 1 introduces the motivation and the objective along with the research questions of the Thesis.

In Chapter 2 the theoretical framework of the elastoplacity and the MCc model is presented. In addition, the extensions of the new model are discussed along with the motivation of them.

Chapter 3 provides an overview of the methodology of analyzing globally the results of the numerical triaxial tests. Moreover, some preliminary analyses are performed to establish the appropriate flow rule.

Chapter 4 investigates the influence of the mixed hardening law in a critical state model in single element tests.

Chapter 5 addresses the incorporation of the new constitutive model in LAGAMINE. Furthermore, the results of the simulations on TxCU and TxCD are discussed and summarized.

Finally, Chapter 6 concludes with a summary and outlooks for future works.

Chapter 2

Literature review

2.1 Introduction

The purpose of this chapter is to present the basic theoretical background knowledge utilized in the Thesis. First, the elastoplasticity theory and the Modified Cam clay (MCc) model are presented, as the proposed model is based on this well-established framework. Following up, the shortcomings of the MCc are demonstrated. In addition, methods of addressing these disadvantages are introduced so as the proposed model to be able to predict the mechanical response of the material under investigation.

2.2 Constitutive Modelling

2.2.1 Elasticity

The simpler idealization of soil behavior employed in the constitutive modelling involves the use of elastic law. The basic elastic law adopted before yielding is the generalized Hooke's law assuming the stresses are uniquely determined by the strains, which are totally recoverable. Two parameters, Young's modulus E' and Poisson's ratio ν', are needed to describe the elastic behavior of a homogeneous isotropic material. For soil, it is preferable to use the two more fundamental parameters: bulk modulus K and shear modulus G to describe elastic behaviour, so that the elastic deformation to be distinguished into a volumetric and distortional part respectively. These parameters can be either linear on non-linear functions of the applied effective stresses. Hence, the stress strain relationships are as follows:

$$d\sigma' = \mathbf{D} d\varepsilon \tag{2.1}$$

where:

$$d\sigma' = \begin{bmatrix} d\sigma'_x & d\sigma'_y & d\sigma'_z & d\tau_{xy} & d\tau_{yz} & d\tau_{zx} \end{bmatrix}^T$$

$$d\varepsilon = \begin{bmatrix} d\varepsilon_x & d\varepsilon_y & d\varepsilon_z & d\gamma_{xy} & d\gamma_{yz} & d\gamma_{zx} \end{bmatrix}^T$$

$\mathbf{D}$: is the elastic stiffness matrix

The elastic stiffness matrix **D** can be expressed as the following:

$$\mathbf{D} = \begin{bmatrix} \mathrm{K}+\frac{4}{3}\mathrm{G} & \mathrm{K}-\frac{2}{3}\mathrm{G} & \mathrm{K}-\frac{2}{3}\mathrm{G} & 0 & 0 & 0 \\ \mathrm{K}-\frac{2}{3}\mathrm{G} & \mathrm{K}+\frac{4}{3}\mathrm{G} & \mathrm{K}-\frac{2}{3}\mathrm{G} & 0 & 0 & 0 \\ \mathrm{K}-\frac{2}{3}\mathrm{G} & \mathrm{K}-\frac{2}{3}\mathrm{G} & \mathrm{K}+\frac{4}{3}\mathrm{G} & 0 & 0 & 0 \\ 0 & 0 & 0 & \mathrm{G} & 0 & 0 \\ 0 & 0 & 0 & 0 & \mathrm{G} & 0 \\ 0 & 0 & 0 & 0 & 0 & \mathrm{G} \end{bmatrix} \tag{2.2}$$

The relationships coupling effective bulk modulus K and shear modulus G with Young's modulus E' and Poisson's ratio ν' are as follows:

$$K = \frac{E'}{3(1-2\nu')} \tag{2.3}$$

$$G = \frac{E'}{2(1+\nu')} \tag{2.4}$$

For sake of simplicity, the elastic response can be fully uncoupled into the volumetric and deviatoric deformation using bulk modulus K and shear modulus G in the triaxial stress space under triaxial test conditions as:

$$\begin{bmatrix} d\varepsilon_p^e \\ d\varepsilon_q^e \end{bmatrix} = \begin{bmatrix} \frac{1}{K} & 0 \\ 0 & \frac{1}{3G} \end{bmatrix} \begin{bmatrix} dp' \\ dq \end{bmatrix} \tag{2.5}$$

where:

$$p' = \frac{\sigma_1' + 2\sigma_3'}{3} \tag{2.6}$$

$$q = \sigma_1' - \sigma_3' \tag{2.7}$$

$$d\varepsilon_p = d\varepsilon_1 + 2d\varepsilon_3 \tag{2.8}$$

$$d\varepsilon_q = \frac{2}{3}(d\varepsilon_1 - d\varepsilon_3) \tag{2.9}$$

p' is the mean effective stress, q is the deviatoric stress, $d\sigma'_{1,3}$ is the effective stress increment in principal directions, $d\varepsilon_p$ is the volumetric strain increment, $d\varepsilon_q$ is the deviatoric strain increment, $d\varepsilon'_{1,3}$ is the strain increment in principal directions and the superscript e denotes elastic component.

Despite the elastic laws being easy and simple to use, they are unable to predict the real soil behavior, as the soil deforms purely elastically in shear strains less than 10^{-5}, making them useful in rough approximations in engineering practice.

2.2.2 Critical State

The Critical State theory developed in the 1960s based on the pioneer work of Roscoe et al. (1958) and it is a fundamental theory for developing elastoplastic constitutive models. Three

parameters are needed to describe the soil state in the conventional triaxial space, namely p', q and the specific volume v, i.e. the volume of soil containing unit volume of solid material, v=1+e. The Critical State concept states that upon shearing the soil material changes its volume (either expansion or contraction) depending on its initial state described by the above parameters, until it reaches a critical void ratio where the soil flows as a frictional fluid (Schofield and Wroth, 1968), and subsequently, no volumetric change is observed despite the continuous shearing. This state is called Critical State where any further distortional strain does not cause any change in mean effective stress p', deviatoric stress q or specific volume v, so as the following to apply:

$$\frac{d\varepsilon_p}{d\varepsilon_q} = \frac{dq}{d\varepsilon_q} = \frac{dp'}{d\varepsilon_q} = 0 \tag{2.10}$$

According to Schofield and Wroth (1968) the well-defined critical state of a soil is determined by two unique equations:

$$q = Mp' \tag{2.11}$$

$$v = \Gamma - \lambda \ln p' \tag{2.12}$$

where:

M : is the slope of CSL in p'-q space, related with the friction angle of soil

Γ : is the intercept of CSL with v axis in v-ln p' space

λ : is the soil compression index

Also, in the same basis it is assumed that under isotropic compression the isotropic normal compression line (NCL) depicts the plastic compression of normally consolidated soils. In addition, the unloading and reloading of a soil is idealized by unique k-lines (URL). The two unique equations are as follows respectively:

$$v = N - \lambda \ln p' \tag{2.13}$$

$$v = v_\kappa - \kappa \ln p' \tag{2.14}$$

where:

N : is the specific volume when p'=1kPa

v_κ : is dependent on stress history

κ : is the soil swelling index

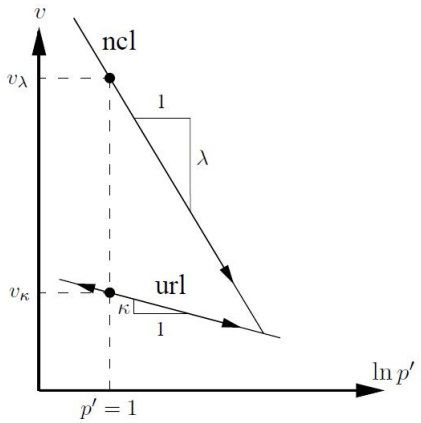

Figure 2.1: Normal Compression Line (NCL) and Unloading-Reloading Line (URL) on the compression plane ($\ln p'$: v)

2.2.3 Elastoplasticity

As it was mentioned in Section 2.2.1 elastic models are rarely accurate in predicting the soil behavior. Thus, the concept of elastoplasticity becomes relevant in understanding the material response. In elastoplasticity the strain can be decomposed into recoverable elastic strains $d\varepsilon^e$ and irrecoverable plastic strains $d\varepsilon^p$. Hence, total strains are described by:

$$d\varepsilon = d\varepsilon^e + d\varepsilon^p \tag{2.15}$$

In order to be able to better understand the elastoplastic modelling, the concept of yielding should be explained. The transition from elastic strains to plastic strains is called yielding and may occur for different stress combinations. These stress combinations define the yield points which formulate a surface boundary, namely called yield surface or yield locus. According to Muir Wood (1990) *a yield surface marks the boundary between the region of purely elastic strain to the region with combined elastic and plastic strain.*

Hence, the concepts of elasticity, plasticity and yielding are combined into an elasto-plastic model. In order to define an elasto-plastic model four ingredients should be defined:

- Elastic Properties
- Yield Criterion
- Plastic Potential
- Hardening Rule(s)

Elastic Properties

Deformations inside the yield surface are purely elastic and, thus, obey an elastic law, the one it was described in 2.2.1. In the Eq. (2.5) the volumetric strain and deviatoric strains are de-coupled and are linked with the mean effective stress p' and deviatoric stress q. By rewriting Eq. (2.14) into incremental format, as the elastic volumetric strain can be described by the unloading-reloading lines, one can obtain:

$$dv^e = -\kappa \frac{dp'}{p'} \tag{2.16}$$

By definition the increment of volumetric strain is equal to the change of volume divided by the initial volume:

$$d\varepsilon_p = \frac{-dv}{v} \tag{2.17}$$

By combining Eq.(2.16) and (2.17) the volumetric elastic strain is formulated as:

$$d\varepsilon_p^e = \frac{\kappa dp'}{vp'} \tag{2.18}$$

Thus, the bulk modulus in the elastic region results from combining Eq.(2.5) and (2.18):

$$K = \frac{vp'}{\kappa} \tag{2.19}$$

By combining Eq.(2.3) and (2.20) and assuming a constant Poisson ratio, the shear modulus G, which is necessary for the calculation of elastic deviatoric strains, can be expressed associated with the bulk modulus K as:

$$G = \frac{3(1-2\nu')K}{2(1+\nu')} \tag{2.20}$$

Yield Criterion

The second ingredient for describing an elastoplastic constitutive model is the yield surface. An incremental stress change will lead to the generation of purely elastic strains or elasto-plastic strains depending on the values of yield surface. The material behavior according to the value of yield surface $F(\boldsymbol{\sigma}, \boldsymbol{\kappa})$ is summarized in the Table 2.1:

Table 2.1: Current state of the model

Situation	**State**	**Strains**
$F(\boldsymbol{\sigma}, \boldsymbol{\kappa})>0$	Not Allowable	(-)
$F(\boldsymbol{\sigma}, \boldsymbol{\kappa})<0$	Purely Elastic	$(d\varepsilon=d\varepsilon^e)$
$F(\boldsymbol{\sigma}, \boldsymbol{\kappa})=0$	Elasto-plastic	$(d\varepsilon=d\varepsilon^e+d\varepsilon^p)$

where $\boldsymbol{\kappa}$ is a set of hardening/softening variables controlling the change of size of yield locus. If $\boldsymbol{\kappa}$ is constant, the yield locus is constant and perfect plasticity is utilized. If $\boldsymbol{\kappa}$ is related with plastic strains, hardening/softening plasticity is employed.

Plastic Potential

The plastic potential is the ingredient which controls the direction of plastic strains specifying the relative magnitudes of components of plastic deformation. The plastic potential $Q(\boldsymbol{\sigma}, \boldsymbol{\beta})$ is a function of stresses and the hidden hardening/softening variables which control the size of the plastic potential. The plastic strain increment vector must be orthogonal always to the plastic potential in the outward direction. The plastic potential may coincide with the yield surface resulting to an associated flow rule. In this case the material obeys the postulate of stability through normality (Drucker, 1959). Otherwise, a non-associated flow rule is employed if the plastic potential differs from the yield surface. The plastic response, in general, can be expressed as:

$$d\varepsilon^p = d\lambda \frac{dQ}{d\boldsymbol{\sigma}} \tag{2.21}$$

Hardening Rule

The hardening rule is the last ingredient necessary for the full description of an elasto-plastic model. The hardening law defines the absolute magnitude of the plastic strains by linking them with the changing size/shape of the yield surface. This rule prescribes how the hidden variables $\boldsymbol{\kappa}$ vary with plastic strains through the plastic multiplier $d\lambda$ of Eq. (2.21). The hardening law may be isotropic, depending on the volumetric plastic strains (volumetric hardening), on the deviatoric plastic strains (deviatoric hardening) or on a combination of previously referred strains, kinematic or mixed.

2.2.4 The General Elastoplastic Model

By using the theory outlined in Section 2.2.3, the general formulation of an elasto-plastic model can be presented. By differentiating the yield function $F(\boldsymbol{\sigma}, \boldsymbol{\kappa})$ and considering that its increment must obey the consistency condition, it yields:

$$dF = \left\{ \frac{\partial F}{\partial \boldsymbol{\sigma}} \right\}^T d\boldsymbol{\sigma} + \left\{ \frac{\partial F}{\partial \boldsymbol{\kappa}} \right\}^T d\boldsymbol{\kappa} = 0 \tag{2.22}$$

The Eq. (2.22) may be rewritten to:

$$\left\{ \frac{\partial F}{\partial \boldsymbol{\sigma}} \right\}^T d\boldsymbol{\sigma} - A d\lambda = 0 \tag{2.23}$$

where A is the plastic modulus:

$$A = -\left(\left\{ \frac{\partial F}{\partial \boldsymbol{\kappa}} \right\}^T \cdot \left\{ \frac{d\boldsymbol{\kappa}}{d\lambda} \right\} \right) = -\left(\left\{ \frac{\partial F}{\partial \boldsymbol{\kappa}} \right\}^T \cdot \left\{ \frac{d\boldsymbol{\kappa}}{d\varepsilon^p} \right\} \left\{ \frac{d\varepsilon^p}{d\lambda} \right\} \right) \tag{2.24}$$

Substituting Eq. (2.21) into the Eq. (2.24), the plastic modulus can be rewritten as:

$$A = -\left(\left\{ \frac{\partial F}{\partial \boldsymbol{\kappa}} \right\}^T \cdot \left\{ \frac{d\boldsymbol{\kappa}}{d\varepsilon^p} \right\} \left\{ \frac{\partial Q}{\partial \boldsymbol{\sigma}} \right\} \right) \tag{2.25}$$

Solving for the plastic multiplier $d\lambda$, the Eq. (2.23) yields:

$$d\lambda = \frac{1}{A} \left\{ \frac{\partial F}{\partial \boldsymbol{\sigma}} \right\}^T d\boldsymbol{\sigma} \tag{2.26}$$

Substituting Eq. (2.1) and (2.21) along with Eq. (2.26) into Eq. (2.15), the decomposition equation returns:

$$d\varepsilon = D^{-1} d\boldsymbol{\sigma} + \frac{1}{A} \left\{ \frac{\partial Q}{\partial \boldsymbol{\sigma}} \right\} \left\{ \frac{\partial F}{\partial \boldsymbol{\sigma}} \right\}^T d\boldsymbol{\sigma} \tag{2.27}$$

which may be formulated in compact form as:

$$d\varepsilon = D_{ep}^{-1} d\boldsymbol{\sigma} \quad \text{where} \quad D_{ep}^{-1} = D^{-1} + \frac{1}{A} \left\{ \frac{\partial Q}{\partial \boldsymbol{\sigma}} \right\} \left\{ \frac{\partial F}{\partial \boldsymbol{\sigma}} \right\}^T \tag{2.28}$$

Introducing the Eq. (2.28) in terms of p' and q yields to:

$$\begin{bmatrix} d\varepsilon_p^e \\ d\varepsilon_q^e \end{bmatrix} = \begin{bmatrix} \frac{1}{K} & 0 \\ 0 & \frac{1}{3G} \end{bmatrix} \begin{bmatrix} dp' \\ dq \end{bmatrix} \tag{2.29a}$$

$$\begin{bmatrix} d\varepsilon_p^p \\ d\varepsilon_q^p \end{bmatrix} = \frac{-1}{\frac{\partial F}{\partial \boldsymbol{\kappa}} \left(\frac{\partial \boldsymbol{\kappa}}{\partial \varepsilon_p^p} \frac{\partial Q}{\partial p'} + \frac{\partial \boldsymbol{\kappa}}{\partial \varepsilon_q^p} \frac{\partial Q}{\partial q} \right)} \begin{bmatrix} \frac{\partial F}{\partial p'} \frac{\partial Q}{\partial p'} & \frac{\partial F}{\partial q} \frac{\partial Q}{\partial p'} \\ \frac{\partial F}{\partial p'} \frac{\partial Q}{\partial q} & \frac{\partial F}{\partial q} \frac{\partial Q}{\partial q} \end{bmatrix} \begin{bmatrix} dp' \\ dq \end{bmatrix} \tag{2.29b}$$

The Eq. (2.29b) is referred as compliance matrix and is activated only if the yield criterion is violated and plastic strains are occurring. If the flow rule is associated (F=G), then the compliance matrix is symmetrical.

In numerical modelling, the incremental stresses are more conveniently determined through the strain and stiffness matrix and, thus, the elastoplastic matrix should be derived as:

$$d\boldsymbol{\sigma} = D d\varepsilon^e \tag{2.30}$$

and substituting the elastic strains $d\varepsilon^e$ from the decomposition equation and the plastic strains $d\varepsilon^p$ from Eq. (2.21) it yields:

$$d\boldsymbol{\sigma} = D(d\varepsilon - d\varepsilon^p) = D d\varepsilon - D d\lambda \frac{\partial Q}{\partial \boldsymbol{\sigma}} \tag{2.31}$$

Inserting Eq. (2.31) into the consistency equation (2.23) the plastic multiplier $d\lambda$ may be rewritten as:

$$d\lambda = \frac{\left\{ \frac{\partial F}{\partial \boldsymbol{\sigma}} \right\}^T D d\varepsilon}{A + \left\{ \frac{\partial F}{\partial \boldsymbol{\sigma}} \right\}^T D \left\{ \frac{\partial Q}{\partial \boldsymbol{\sigma}} \right\}} \tag{2.32}$$

Substituting the expression for $d\lambda$ from Eq. (2.32) into Eq. (2.31) furnishes the standard elastoplastic stress-strain relations of the form:

$$d\boldsymbol{\sigma} = D_{ep} d\varepsilon \quad \text{where} \quad D_{ep} = D - \frac{D \left\{ \frac{\partial Q}{\partial \boldsymbol{\sigma}} \right\} \left\{ \frac{\partial F}{\partial \boldsymbol{\sigma}} \right\}^T D}{A + \left\{ \frac{\partial F}{\partial \boldsymbol{\sigma}} \right\}^T D \left\{ \frac{\partial Q}{\partial \boldsymbol{\sigma}} \right\}} \tag{2.33}$$

2.2.5 Modified Cam clay

The modified Cam-clay model was developed by Roscoe and Burland (1968) as an extension of the original Cam-clay model of Roscoe et al. (1963) in order to estimate the soil response during triaxial test. This model successfully reproduces the major deformation characteristics of soft clay and is more widely used for numerical predictions than the original Cam-clay model.

The MCc model uses the basic concepts of elastoplastic models as these have been thoroughly described. More specifically, these principles are listed as:

1. The recoverable plastic and shear strains are only dependent on p' and q respectively and described be Eq. (2.29a).

2. The associative flow rule is a major concept of the model (Q=F).

3. The hardening variable of the model is the preconsolidation pressure (κ=p_0)

Thus, the yield function can be formulated in the triaxial space as:

$$F(p', q, p_0) = 0 \qquad\qquad F = q^2 - M^2(p'(p'_0 - p')) \tag{2.34}$$

In order to present the stress strain relationship of the MCc in the form of the compliance matrix, the derivatives of yield locus F and plastic potential Q with respect to p' and q which are equal as associated flow rule is used, and yield locus F with respect to p_c are derived:

$$\frac{\partial F}{\partial p'} = \frac{\partial G}{\partial p'} = M^2(2p' - p'_0) \tag{2.35a}$$

$$\frac{\partial F}{\partial q} = \frac{\partial G}{\partial q'} = 2q \tag{2.35b}$$

$$\frac{\partial F}{\partial p'_c} = -M^2 p' \tag{2.35c}$$

Regarding the evolution of the preconsolidation pressure with respect to plastic strains, only the volumetric plastic strains contribute to the expansion of the yield locus. Therefore, the MCc is known as a volumetric hardening model. For determining the evolution of preconsolidation pressure dp'_0 with the increment of plastic volumetric stain $d\varepsilon^p_p$, the compression and swelling equations should be recalled. Considering that the swelling line expresses the elastic volume change and the compression line the total volume change, the plastic volume change comes from their difference. Hence, the increment of plastic volumetric strain $d\varepsilon^p_p$ is derived by subtracting the differential form of Eq. (2.13) with the differential form of Eq. (2.14) and then by relating the increment of plastic strain with the volume change through Eq. (2.17).The above are presented below:

$$dv^p = -(\lambda - \kappa)\frac{dp'_0}{p'_0} \tag{2.36}$$

$$d\varepsilon^p_p = (\lambda - \kappa)\frac{dp'_c}{vp'_0} \tag{2.37}$$

Therefore, the dependence of plastic strains $d\varepsilon^p$ with the preconsolidation pressure dp'_0 may be written as:

$$\frac{d\varepsilon^p_p}{dp'_0} = \frac{\lambda - \kappa}{vp'_0} \tag{2.38a}$$

$$\frac{d\varepsilon^p_q}{dp'_0} = 0 \tag{2.38b}$$

The yield function can be reformulated in terms of the stress ratio η (η=$\frac{q}{p'}$) as:

$$\frac{p'}{p'_0} = \frac{M^2}{M^2 + \eta^2} \tag{2.39}$$

Combining Eq. (2.35), (2.38) and (2.39) and substituting them into the general plastic constitutive relationship (2.29b) the compliance matrix for the MCc becomes:

$$\begin{bmatrix} d\varepsilon^p_p \\ d\varepsilon^p_q \end{bmatrix} = \frac{(\lambda - \kappa)}{vp'(M^2 + \eta^2)} \begin{bmatrix} (M^2 - \eta^2) & 2\eta \\ 2\eta & \dfrac{4\eta^2}{(M^2 - \eta^2)} \end{bmatrix} \begin{bmatrix} dp' \\ dq \end{bmatrix} \tag{2.40}$$

Shortcomings of Modified Cam clay

Herein, the shortcomings of MCc model, which can be relevant to the observed peat behavior reported in Chapter 1, are outlined:

1. The MCc model does not include any anisotropic characteristic in its formulation as it is based on the assumption that soils are isotropic. However, peat exhibits a predominant anisotropic behavior due to its deposition mode and its high fiber content.
2. Creep, an important feature of peat deposits, cannot be modelled by MCc model.
3. The predicted behavior of heavily overconsolidated clay (i.e states to the left side of the critical state line, 'dry' side) is quite poor as the yield surface adopted in this model is problematic in this side.
4. The behavior of granular materials is not successfully modelled as the sand does not obey in the principle of normality. Therefore, a non-associated flow rule should be adopted for capturing the mechanical response of granular materials so as the critical state point not to lie at the top of the yield locus (Chandler, 1990). This drawback becomes relevant with the goal of modelling the peat behavior as the plastic potential suitable for peats may not coincide with the yield function.
5. The contribution of plastic shear strains in the evolution of yield function cannot always be neglected and the shear hardening should be included in the volumetric hardening law of MCc model (Nova, 1977).

To overcome these shortcomings, a large number of modifications have been proposed by various researchers. More specifically, the integration of anisotropic yield surfaces in the MCc model has been proposed by Ohta and Wroth (1976) and Whittle (1993). For dealing with the rate dependency of geomaterials Borja and Kavazanjian (1985) and Yin and Graham (1999) researched on the creep behavior of clays. For overcoming the problems on the 'dry' side, the Hvorslev surface is used as the yield function in this region (Atkinson and Bransby, 1977), rendering this treatment problematic as two separate yield surfaces are used and a discontinuity which may cause considerable numerical difficulties is created. Finally, the critical state modelling of sand (Nova and Wood, 1979) incorporating the deviatoric hardening and the non-associated flow rule is partially successful as the yield surfaces for sands seems to be different than those for clays (Nova and Wood, 1978) and insufficient data for the determination of the critical state and normal consolidation lines of sands was available (Atkinson and Bransby, 1977).

Despite the aforementioned modifications introduced in the MCc model , there are still limitations as Gens and Potts (1988) state, where they note that the large amount of introduced constants in the models without a clear physical meaning and the numerical problems associated with the adaptation of two separate yield surfaces for dealing with the poor performance of critical state models in the 'dry' side render these modifications inadequate in the wide engineering practice.

2.2.6 Background of the proposed modifications

As it has been already mentioned in the scope of the Thesis , the proposed model will not deal with strain rate modelling of peat and anisotropic yield surfaces. The proposed model follows the philosophy adopted by Yu (1998) in the CASM model, where there is a limited amount of material constants which are easily determined and a single yield function and plastic potential are used. The suggested alterations following the same concept as above which will be added in and modify the MCc model are discussed below.

Generalized Shapes of Yield Locus and Plastic Potential

The implementation of versatile yield surfaces and plastic potentials in the constitutive models, which will represent accurately the ones observed experimentally, is critical for modelling successfully real soil behavior. Towards this adoption of concept, various equations for describing the shapes of yield locus and plastic potentials have been proposed by various researchers (Lagioia et al., 1996; Yu, 1998; McDowell and Hau, 2004). In this Thesis, the equations proposed by McDowell and Hau (2004) constitute the basis for extending the MCc model. The reasoning behind this choice lies to the concept of using a minimum number of additional parameters with an easy way of determining them and of having less theoretical shortcomings. In essence, the expressions from McDowell and Hau (2004) have less new additional parameters than the expressions of Lagioia et al. (1996). Correspondingly, the handicap observed in the CASM model of Yu (1998) where Rowe's stress-dilatancy relationship (Rowe, 1962) is implemented, which predicts non associated flow under isotropic conditions, behavior contradicting the findings of literature as stated in McDowell and Hau (2004), is not present in the selected expression.

The flow rule in this model is given by:

$$\frac{d\varepsilon_p^p}{d\varepsilon_q^p} = \frac{M^2 - \eta^2}{k_g \eta} \tag{2.41}$$

which is the same as Ohmaki (1982) has proposed. By integrating the flow rule, the expression for yield surface and plastic potential for $k_{f,g} \neq 1$ becomes:

$$q^2 = -\frac{M_f^2}{1 - k_f}\left(\frac{p'}{p'_0}\right)^{\frac{2}{k_f}} p_0'^2 + \frac{M_f^2 p'^2}{1 - k_f} \tag{2.42}$$

$$q^2 = -\frac{M_g^2}{1 - k_g}\left(\frac{p'}{p'_p}\right)^{\frac{2}{k_g}} p_p'^2 + \frac{M_g^2 p'^2}{1 - k_g} \tag{2.43}$$

where M_f and M_g intersect the yield locus and plastic potential at their apex, k_f and k_g control the shape of the yield surface and plastic potential, p_0 is the preconsolidation pressure controlling the size of yield surface and p_p is the corresponding hidden variable for the plastic potential. Figure 2.2a presents the influence of $k_{f,g}$ on the shape of locus, where a locus with low values of $k_{f,g}$ is skewed to the right while a locus with high values of $k_{f,g}$ is skewed to the left. Note that for $k_{f,g} = 2$ one can retrieve surfaces of MCc model. The effect of M is well known as it controls the steepness of a surface (Figure 2.2b).

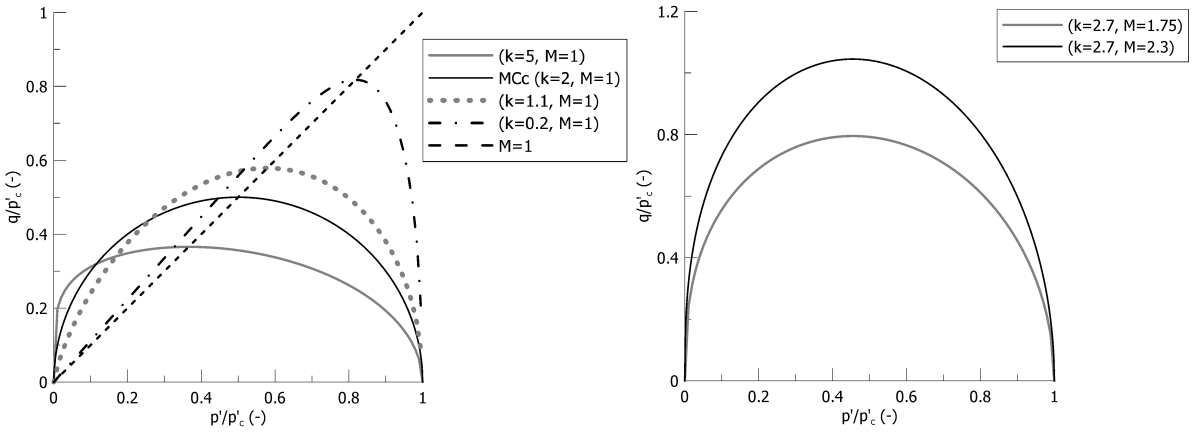

(a) Effect of k in the shape of yield locus/plastic potentials

(b) Effect of M in the steepness of yield locus/plastic potentials

Figure 2.2: Yield locus/plastic potentials of the model

Deviatoric Hardening

Looking into the stress paths from TxCU tests in peat presented in Chapter 1, one can observe a ″hook″ as it is observed in sands under similar test conditions. With a volumetric hardening law, this behavior cannot be predicted. Based on the pioneer work of Nova (1977) the hardening law can be extended so as the plastic deviatoric strains $d\varepsilon_q^p$ to contribute to the change of size of preconsolidation pressure. Thus, this combined hardening law can be written as:

$$dp_0' = \frac{vp_0'}{\lambda - \kappa}(d\varepsilon_p^p + Dd\varepsilon_q^p) \tag{2.44}$$

The D is a parameter which controls the amount of contribution of plastic deviatoric strains $d\varepsilon_q^p$ in the evolution of the preconsolidation pressure p_0'. However, the inclusion of plastic deviatoric strains in the hardening law ($D \neq 0$) has an effect in the stress obliquity at failure (Lagioia and Panteghini, 2014). In particular, critical state implies:

$$d\varepsilon_p^p + Dd\varepsilon_q^p = 0 \tag{2.45}$$

and in contradiction with the Critical State theory failure occurs for a non-null dilatancy:

$$d_f = \frac{d\varepsilon_p^p}{d\varepsilon_q^p} = -D \tag{2.46}$$

Using the flow rule of Eq. 2.41 the stress ratio at failure is related with the dilatancy at failure after some derivations as:

$$\eta_f = \frac{Dk_g}{2} + \frac{\sqrt{D^2k_g^2 + 4M_g^2}}{2} \tag{2.47}$$

The latter equation indicates that the stress ratio at failure is larger than the one defined by the M_g parameter when a combined hardening law is used. Moreover, the value of stress obliquity depends on the chosen plastic potential through the parameter k_g.

In order to eliminate the influence of D on the value of stress obliquity at failure, the D can be a function of cumulative plastic deviatoric strains (Wilde, 1977). More particularly, it may decrease exponentially with the increase of plastic deviatoric strains.

$$D = D_0 e^{-D_1 \varepsilon_q^p} \tag{2.48}$$

so as at failure where the plastic shear strains are maximized ($D \to 0$) the stress ratio to be equal with M_g.

The D_0 and D_1 parameters indicate the initial value of D and the decrease rate related with the cumulative plastic deviatoric strains respectively. Their values can be calibrated by the parameter α which links the change of deviator stress with the change of mean effective stress:

$$\alpha = -\frac{dp'}{dq} \tag{2.49}$$

Then, the principle of effective stresses in incremental form yields:

$$du = dp + \alpha dq \tag{2.50}$$

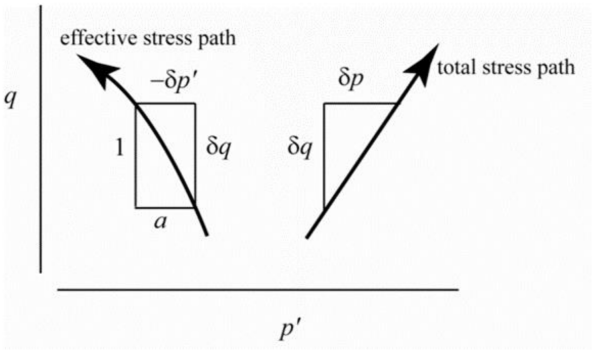

Figure 2.3: Generation of pore pressure from changes in total and effective mean stresses (adopted from Muir Wood (1990))

Extension to the Three-Dimensional Stress Space

In the previous sections, the yield surfaces and plastic potentials have been presented in the triaxial stress space. For a generalized 3D state the p' and q should be redefined. In addition, the $M_{f,g}$ now depends on the Lode angle θ. In the 3D stress space the following equations apply:

$$p' = \frac{\sigma'_x + \sigma'_y + \sigma'_z}{3} = \frac{I_1}{3} \tag{2.51}$$

$$q = \sqrt{3} J_2 \tag{2.52}$$

$$\theta = -\frac{1}{3} \sin^{-1}\left(\frac{3\sqrt{3}}{2} \frac{\det s}{J_2^3}\right) \tag{2.53}$$

where:

$$J_2 = \sqrt{\frac{1}{2} s_{ij} s_{ij}} \tag{2.54}$$

$$J_3 = \frac{1}{3} s_{ij} s_{jk} s_{ki} \tag{2.55}$$

$$s_{ij} = \sigma_{ij} - \frac{I_1}{3} \delta_{ij} \tag{2.56}$$

$$\delta_{ij} = \begin{cases} 0 & i \neq j \\ 1 & i = j \end{cases} \tag{2.57}$$

Hence, the expressions for the yield surface and plastic potential are modified as:

$$3J_2^2 = -\frac{M^2_{(f,g)_\theta}}{1 - k_{f,g}} \left(\frac{I_1}{3p'_0}\right)^{\frac{2}{k_{f,g}}} + \frac{M^2_{(f,g)_\theta} I_1^2}{9(1 - k_{f,g})} \tag{2.58}$$

As far as the $M_{(f,g)_\theta}$ is concerned, its dependency with Lode angle θ determines the shape of yield surface and plastic potential in the deviatoric plane. Amongst the various formulations proposed by various researchers (Drucker and Prager, 1952; Matsuoka and Nakai, 1974; van Eekelen, 1980; Sheng et al., 2000), the van Eekelen model is adopted in this Thesis.

More specifically, (see Dieudonné, 2016) the critical state line $M_{(f,g)_\theta}$ is written as:

$$M_{(f,g)_\theta} = a(1 + b \sin 3\theta)^n \tag{2.59}$$

where a, b and n are parameters. The parameter n is a constant related with the convexity of the surface in the deviatoric plane and is equal to -0.229. a and b depend on the triaxial compression and extension friction angles, ϕ_C and ϕ_E respectively and are equal to:

$$a = \frac{r_C}{(1+b)^n} \quad \text{and} \quad b = \frac{\left(\frac{r_C}{r_E}\right)^{\frac{1}{n}} - 1}{\left(\frac{r_C}{r_E}\right)^{\frac{1}{n}} + 1} \tag{2.60}$$

where r_C and r_E are the reduced radii for axisymmetric triaxial stress paths of compression and extension:

$$r_C = \frac{2\sin\phi_C}{\sqrt{3}(3-\sin\phi_C)} \quad \text{and} \quad r_E = \frac{2\sin\phi_E}{\sqrt{3}(3+\sin\phi_E)} \tag{2.61}$$

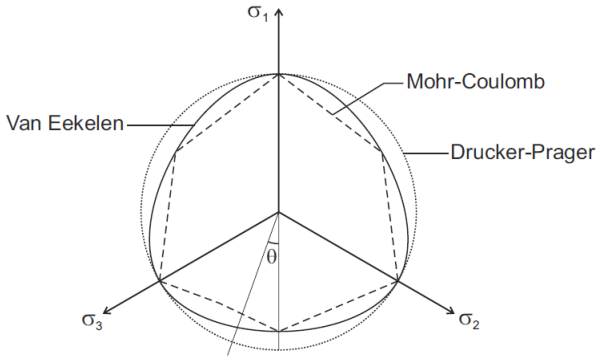

Figure 2.4: Limit surfaces for Mohr-Coulomb, Drucker-Prager and Van Eekelen criteria in the deviatoric plane

Chapter 3

Preliminary study with MCc model

3.1 General

The purpose of this chapter is to investigate at which extent a basic constitutive model, as Modified Cam clay with associative or non-associative plasticity, is adequate to capture the pre-failure behavior of peat as observed in standard laboratory procedures. The comparison is done in terms of boundary value problem by simulating the real conditions during a triaxial tests with FEM analysis. The validation of the FEM model follows and, finally numerical simulations are presented in comparison with experimental results which demonstrate the limitations of the used constitutive model and the urgency of adding the necessary ingredients, discussed in Chapter 2, in the new constitutive model.

3.2 Finite Element Model

3.2.1 Constitutive Model of Soil

The preliminary analyses aim at investigating to which extent the use of Modified Cam clay with an associated or non-associated flow rule can capture the peat behavior from triaxial tests. The non-associated flow rule proposed by Ohmaki (1982) and later by Alonso et al. (1990) is used in these preliminary analyses to allow sufficient flexibility of the model. The determination of the parameters of this flow rule and its correlation with the parameters of the flow rule described in Chapter 2 is provided later on this Thesis.

3.2.2 Soil Platen Interaction

Two types of boundary conditions were chosen to simulate the end platens used in triaxial tests. Either there is a perfectly smooth contact where no friction is developed between the specimen and end platens or a completely rough contact is employed where no sliding is allowed. The first type of contact is modeled by fixing only the vertical degree of freedom and setting free the horizontal degree of freedom of top and bottom boundaries of the sample. This type of boundary condition is known as Roller Boundary Condition. The second type of contact is modeled by introducing a stiffer element at bottom and top of the sample which will forbid due to the developing friction the horizontal displacement of the bottom and of the top nodes of the sample material and will not contribute to the vertical displacement of the sample due to its comparatively high stiffness with the sample stiffness.

3.2.3 Mesh Properties

2D axisymmetric analyses were run. The x-y plane of the triaxial specimen is discretized into 8-node biquadratic elements every 1 mm of soil sample with pore pressure as the third degree of freedom. This element can be used also for modeling the large deformations of the soil as it employs non-linear geometrical features. The y-axis in the one of symmetry for the soil specimen. Depending on the simulated test (stress or strain control, compression or extension tests), the top and the right boundary can be subjected to cell pressure or displacements. The drainage from the bottom and top boundaries is allowed in the case of drained test. Figure 3.1 depicts the modelled sample geometry with the two types of contact and applied boundary conditions. The rigid platens are 5 mm and are represented in the blue box in Figure 3.1.

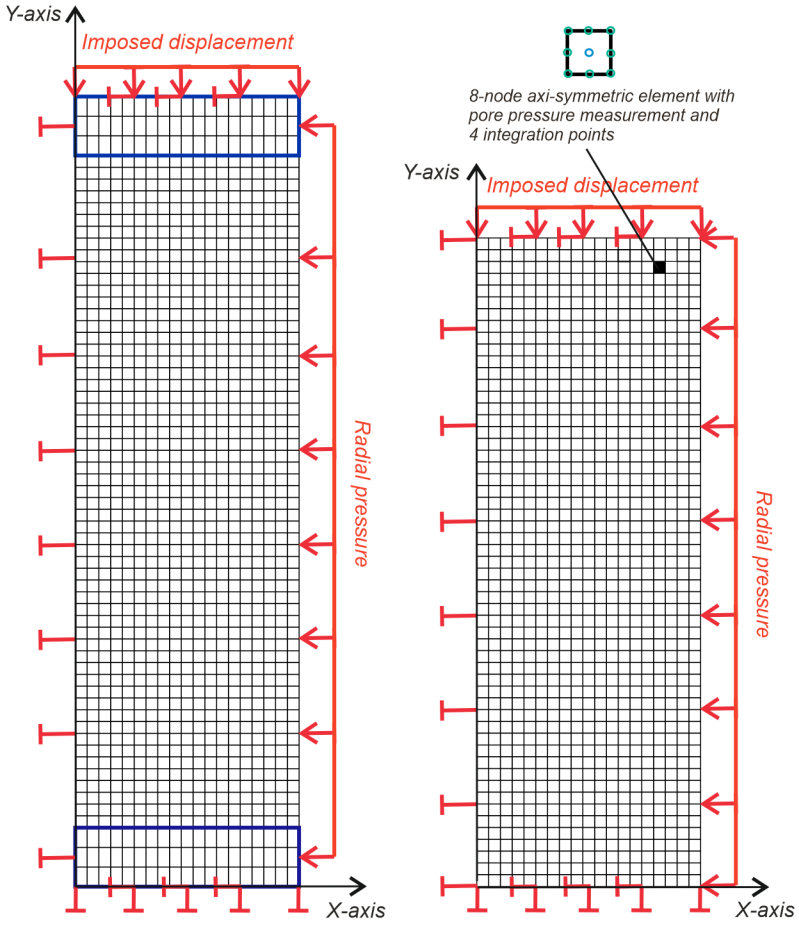

Figure 3.1: Illustrated mesh for the rough and smooth contact type along with applied boundary conditions and 8-node elements

The selected mesh discretization is determined after a series of preliminary analyses for determining the mesh sensitivity. For this scope, rough end platens were simulated due to the occurrence of non-uniform distribution of stresses and strains. The same mesh discretization is chosen also for the smooth contact analyses for consistency reason as a uniform displacement field does not present any space non-linearity so the results in the smooth contact are mesh independent. In the Figure 3.2 it can be seen that after 200 elements the results in terms of stress path and deviatoric stress versus strain converge. Hence, the 1 mm discretization is adequate enough to catch the space non linear phenomena undergoing in triaxial tests with rough end platens. With the selected discretization, the analyses with rough ends and smooth ends take 8 min and 5 min long respectively.

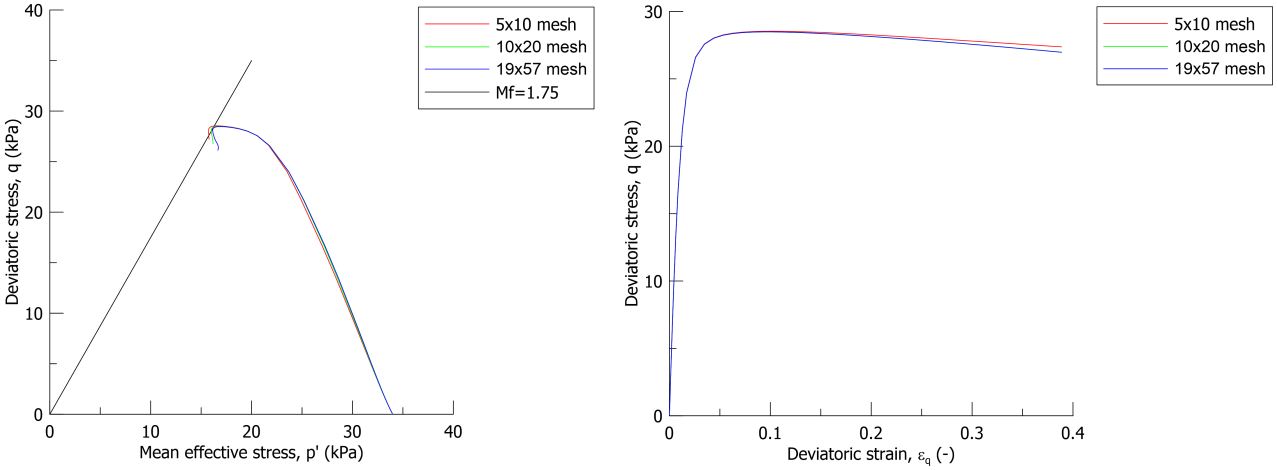

Figure 3.2: Stress path (left) and deviatoric vs strain (right) plots for different mesh discretizations

3.2.4 Global Measures of Stress and Strain

To duplicate the procedure used to elaborate experimental data from triaxial tests, global stresses and strains quantities are used. The global axial stress is computed by dividing the reaction force obtained from the FEM at the top of the sample with 4 alternatives of cross area corrections:

- Nominal diameter of the cap
- Equivalent right cylinder diameter
- Diameter at the 9/10 of height after the suggestion of Sheng et al. (1997)
- Average diameter of the nominal and equivalent right cylinder diameter

As far as the global radial stress is concerned, it is assumed to be equal to the applied cell pressure as it is done in the laboratory (Sheng et al., 1997). Therefore, the global deviatoric stress q and global mean effective stress p' can be calculated as it is described in Chapter 2. The global pore pressure is measured at the bottom boundary of the soil sample as it is traditionally done in the laboratory where a pore pressure probe at mid height of the sample is not installed. Another measurement is also taken at the mid height of the specimen and it is used later on the Thesis. The reason for this is to be explained later. In drained tests, it is assured that the load rate is significant low with respect to the permeability of the soil and, hence, the excess pore water pressures is assumed to be negligible.

With respect to strains, the axial strain is traditionally calculated as the ratio between the measured axial displacement and the initial height of the specimen, known as engineering or infinitesimal strain. In this manner, significant errors are introduced when small strains hypothesis is used in elaborating data from triaxial tests on peat due to large displacement attained by peat samples. Hence, engineering strain is regarded as inadequate and unsuitable for these problems. Another measure is introduced here which can account for the products of displacement derivatives and be suitable for large deformation problems (Onaka, 2012), the natural strain measurement or Hencky strain. In Figure 3.3 the difference between the engineering and natural strain is illustrated. It is observed that for applied strains until 10% the two measurements coincide and for larger strains the deviation increases and the engineering strain can no longer give reliable results.

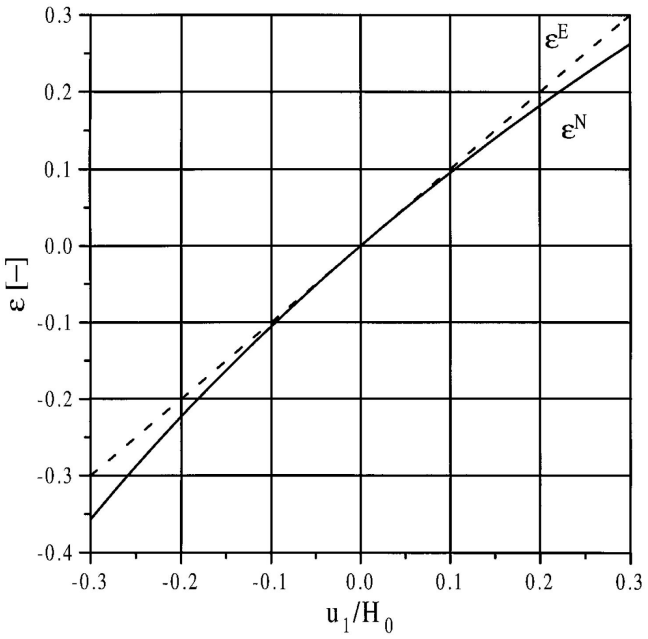

Figure 3.3: Natural versus engineering strain for one-dimensional problem (adopted from Praastrup et al. (1999))

To sum up, the global axial strain $\varepsilon_a^{E,N}$ is equal to the vertical movement of the top platen (u_1) divided by the initial height (E) or equal to the ratio of the current height and initial height of the specimen and associated with the natural logarithm (N). The global radial strain $\varepsilon_r^{E,N}$ is equal to the average radial displacement (u_3) divided by the initial radius (E) or equal to the ratio of the current radius and the initial radius of the specimen and associated with the natural logarithm (N). The average radial displacement is the difference in radii of the initial cross-sectional area and the current cross-sectional area of the volumetrically equivalent right cylinder. It is denoted that the symbol E refers to the engineering strains and N to natural strains. In detail, the above mentioned are depicted below in a mathematical form:

$$\varepsilon_a^E = \frac{u_1}{h_o} \quad \text{and} \quad \varepsilon_a^N = -\ln\frac{h_o - u_1}{h_o} \tag{3.1}$$

$$\varepsilon_r^E = \frac{u_3}{r_o} \quad \text{and} \quad \varepsilon_r^N = -\ln\frac{r_o - u_3}{r_o} \tag{3.2}$$

3.3 Validation

In this Section, the validation of the numerical model is done. The model is tested in comparison with the results from Sheng et al. (1997), where the end restraints effects on triaxial specimens are studied. Strain controlled TxCU test is selected as a reference test. The soil refers to a normal consolidated clay and its properties are given in the Table 3.1. The employed constitutive model is the well known MCc with associated plasticity.

Table 3.1: Parameters of clay from Sheng et al. (1997)

$\boldsymbol{\lambda}$	$\boldsymbol{\kappa}$	$\boldsymbol{\nu'}$	$\boldsymbol{M_g}$	$\boldsymbol{p'_0(kPa)}$	$\boldsymbol{e_0}$	$\boldsymbol{OCR}$	$\boldsymbol{k(m/s)}$
0.2	0.02	0.36	1.2	120	2.5	1	2×10^{-9}

In Figure 3.4, the response from the FEM analyses and the results reported in Sheng et al. (1997) are displayed. The deviatoric stress of a rough test is calculated for both the 4 area corrections from Section 3.2.4. In addition, the stress strain behavior of a smooth test is presented as a comparison measurement for the 4 area corrections. The terms AGSM, EGSM and RGSM from Sheng et al. (1997) correspond to the nominal diameter, equivalent cylinder diameter and diameter at 9/10 of height respectively. It can be seen that stress strain responses with the various area corrections and of the smooth test are in agreement with the reference paper. More specifically, the correction with the nominal diameter overestimates the deviatoric stress, while the correction with equivalent cylinder generates an artificial softening response which is not related to the material behaviour but is implied due to the cross area correction. The average diameter and the diameter at the 9/10 height of the specimen converges with the response from the smooth test where the true material behavior is observed. Hence, one of the conclusion of Sheng et al. (1997), namely the approximation of smooth tests with the diameter at the 9/10 height, is validated herein together with the observations for the other area corrections.

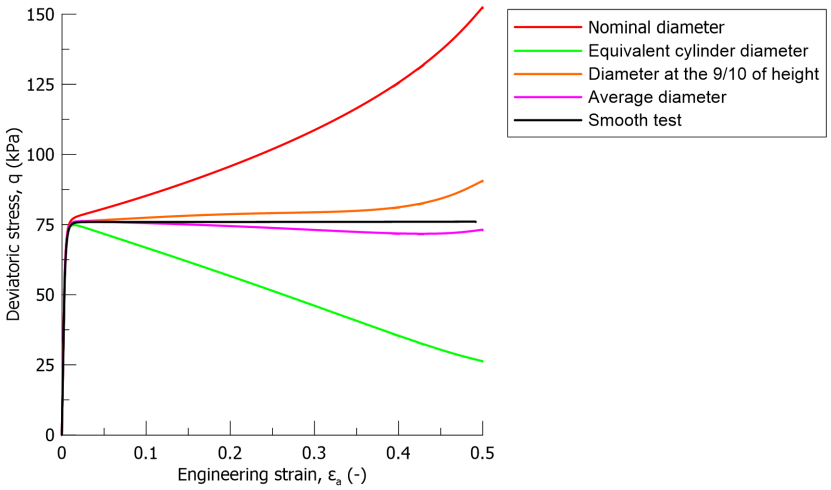

(a) Numerical predictions by LAGAMINE

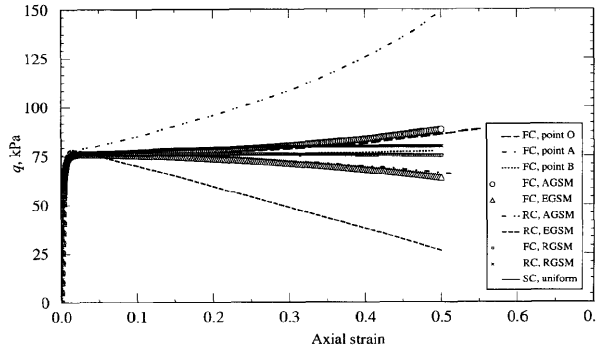

(b) Numerical predictions by Sheng et al. (1997)

Figure 3.4: Deviatoric stress versus axial strain with different area corrections

3.4 Analyses

At this point, the influence of end restraints on the stress-dilatancy rule is investigated. To this end, drained radial stress paths with constant stress ratio q/p' were simulated. The dilatancy d is equal to the ratio of plastic volumetric increment $d\varepsilon_p^p$ and plastic deviatoric increment $d\varepsilon_q^p$:

$$d = \frac{d\varepsilon_p^p}{d\varepsilon_q^p}$$

According to the Critical State theory, dilatancy is infinite at zero stress ratio and becomes null at critical stress ratio. With radial stress tests at different stress ratios, the dilatancy at this stress ratio is obtained. Two series of radial tests are carried out, one using a simple MCc and one using a non associated MCc, based on the flow rule by Ohmaki (1982) and Alonso et al. (1990).

The simulated soil is a reconstituted peat with properties as follows: the initial void ratio $e = 10.4$, the slope of the critical state line $M_g = 1.75$ in a $p' - q$ diagram (corresponding to an internal friction angle $\phi = 42.6°$), the slope of the isotropic normal compression line $\lambda = 2$, the slope of the isotropic unloading and reloading line $\kappa = 0.2$ and Poisson's ratio $\nu' = 0.20$. With respect to hydraulic properties, pure mechanical analyses were run to replicate drained conditions in the lab as non zero excess pore pressures due to a finite rate of strain were not considered. The sample has a radius equal to 19 mm and a height of 76 mm.

Two types of boundaries are used, smooth contact boundaries and rough contacts. In the smooth cases, the obtained stress dilatancy points should lie at the theoretical curves of the implemented flow rules. In rough tests, the various area corrections diverge these points from the theoretical curves. Each analysis have an isotropic loading from 1 kPa to 35 kPa, an unloading path back 15 kPa, then a constant p' stress path until the intended stress ratio, and finally a constant stress ratio path until 100 kPa mean effective stress p' as shown in Figure 3.5. There are in total 5 stress ratios.

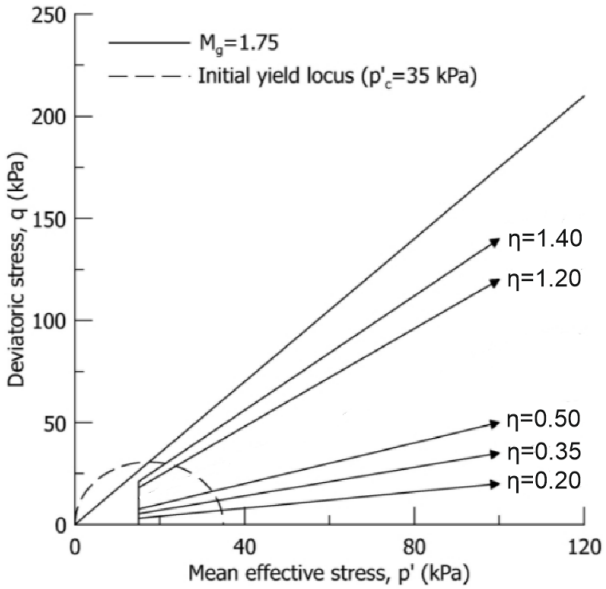

Figure 3.5: Stress histories in numerical simulations

Herein, two aspects of the philosophy behind the analyses should be explained. First, the stress ratios, which the specimen are subjected to, have been selected so as to be below and above of the stress ratio at K_0 conditions because different deformation mechanisms are observed in each condition. For radial paths with $\eta < \eta_{K_0}$, the specimen is under lateral contraction and a uniform deformation at the central portion of the sample is observed (Figure 3.6b). For radial paths above K_0, a bulging of the sample is observed, which results to lateral expansion, and the central part does not show any uniform deformation (Figure 3.6c).

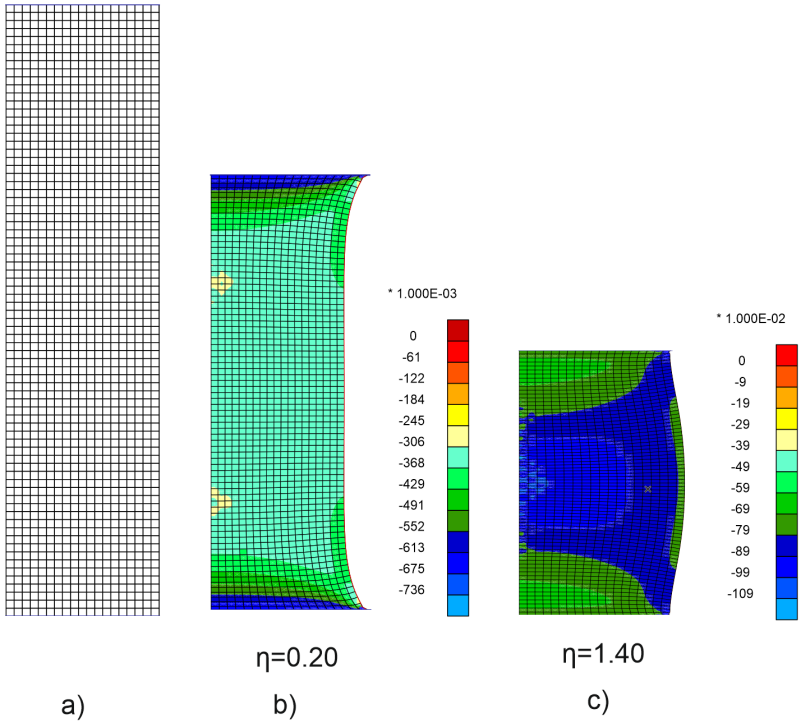

Figure 3.6: Contour plots of the axial strain: a) undeformed configuration; deformed configuration for b) stress ratio $\eta = 0.35$ and c) $\eta = 1.40$

The second aspect to be examined, is related with the selected flow rule and its result to the values of K_0. It is well known that the MCc overestimates the K_0 (Gens and Potts, 1988). The stress ratio at K_0 conditions, according to Equation 10.12 of Muir Wood (1990) and neglecting the elastic strains, is equal to:

$$\eta_{K_0}^2 + 3\eta\frac{\lambda - \kappa}{\lambda} - M_g^2 = 0$$

$$\eta_{K_0} = 0.86$$

This value of η_{K_0} results to a K_0 equal to:

$$K_0 = \frac{3 - \eta_{K_0}}{3 + 2\eta_{K_0}}$$

$$K_0 = 0.45$$

However, the tested material has a friction angle of ϕ' equal to 42.5°. According to Jaky's formula, $K_0 = 1 - \sin\phi'$, the corresponding K_0 value is 0.32, much lower than the prediction from MCc. It should be noted that the applicability of Jaky's equation for normally consolidated

reconstituted peat has been experimentally verified by Muraro and Jommi (2018). Using Eq. (2.41) one can chose a value of k_g in such a way that zero lateral strains along a K_0 path are predicted and consequently giving the realistic value of K_0. By neglecting the elastic strains, and following the procedure outlined in equations 39-42 of Alonso et al. (1990), the k_g is equal to 0.98. Consequently, the stress ratio at K_0 conditions is 1.2.

To sum up, firstly, the stress ratios selected here are below and above the realistic stress ratio at K_0 conditions, and secondly, the non associated flow rule predicts the realistic value of K_0, enhancing the capabilities of the model for predicting the pre-failure behavior of peat.

3.5 Results

Representative area correction

One way to select the representative area correction is to compare the stress-strain response of rough numerical simulations computed with the 4 area corrections with the representative material behavior from smooth tests. In Figure 3.7 this comparison is presented for two radial paths at $\eta = 0.35$ and $\eta = 1.40$, respectively below and above the K_0 stress ratio ($\eta_{K_0} = 0.86$ for the MCc). Figure 3.7 shows that a correction with a volumetrically equivalent right cylinder overestimates the stresses for $\eta < \eta_{K_0}$, while good agreement with the material response is achieved with the correction with average diameter for below K_0 stress paths. Moreover, for stress paths above K_0, both the equivalent cylinder diameter and the average diameter match the smooth stress-strain response in contrast with the findings from Sheng et al. (1997). However, for consistency reasons the average diameter correction is considered as suitable for these stress paths too. Hence, the results will be presenting by correcting the area with the average diameter between the nominal area and the volumetrically equivalent cylinder.

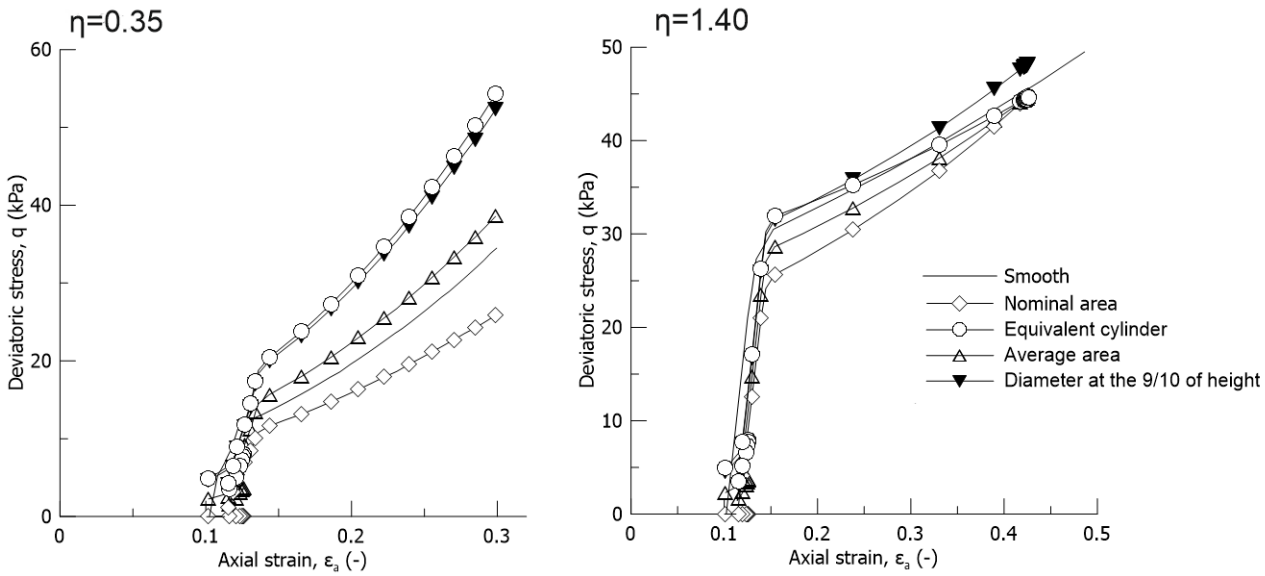

Figure 3.7: Comparison between the deviatoric stress-axial strain response after the four different cross sections corrections and the material response from smooth FE analysis for $\eta = 0.35$ (left) and $\eta = 1.40$ (right)

Associated flow rule

The stress dilatancy points for various stress ratios of rough tests are shown in Figure 3.8 along with the theoretical curve which the associated model obeys. In addition, the Figure depicts the obtained stress dilatancy points of numerical smooth tests which acts as a validating tool for the numerical model. Finally, the graph reports experimental data from drained radial paths performed on reconstituted peat samples from Muraro and Jommi (2018). There is significant deviation between the numerical predictions and experimental results since the associated flow rule predicts higher K_0 value. Thus, peat does not obey to the stress-dilatancy rule predicted by the MCc.

Non associated flow rule

By the same logic, Figure 3.9 presents the obtained stress dilatancy points for the non associated flow rule. Since the generated shear stresses at the end platens reduce the radial contraction and expansion of rough tests compared to smooth conditions, deviations from the theoretical curve are expected. For radial paths below K_0, higher deviatoric strain are expected at a specific stress, while the opposite is noted in radial paths above K_0. As a result, the dilatancy of rough tests below the K_0 is slightly underestimated, while for paths above the K_0 is marginally overestimated. Allowing the K_0 to be predicted correctly, the sample behaviour from the experimental tests is recovered for $\eta < \eta_{K_0}$. For radial paths above the K_0 line, the numerical results are below the experimental ones. For capturing the higher dilatancy at high stress ratios close to critical state, the inclusion of deviatoric hardening in the constitutive model could achieve this as it is shown in Eq. (2.46).

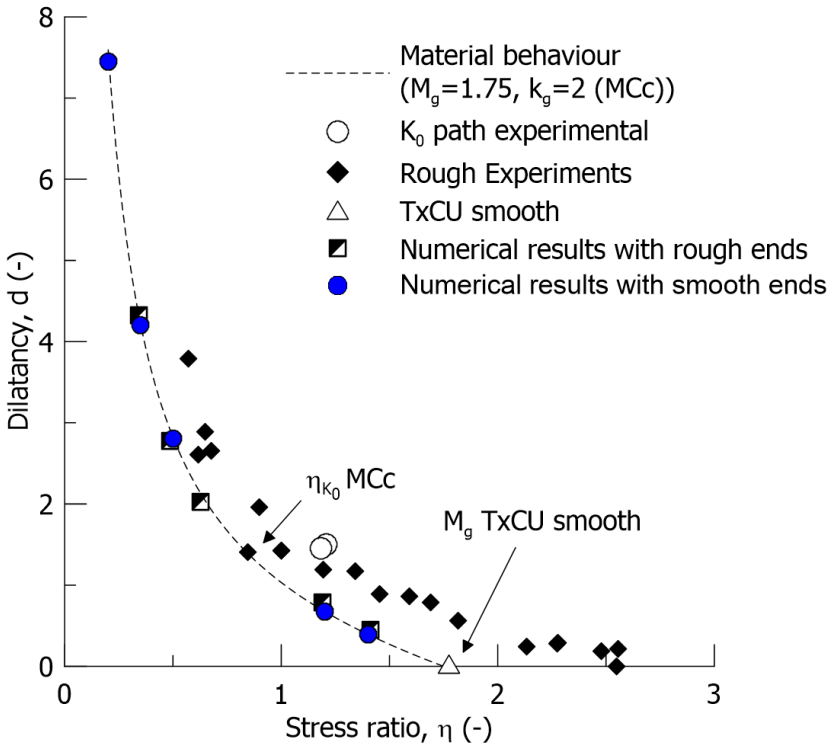

Figure 3.8: Stress-dilatancy relationship d - η for numerical and experimental results compared to the input associated MCc law

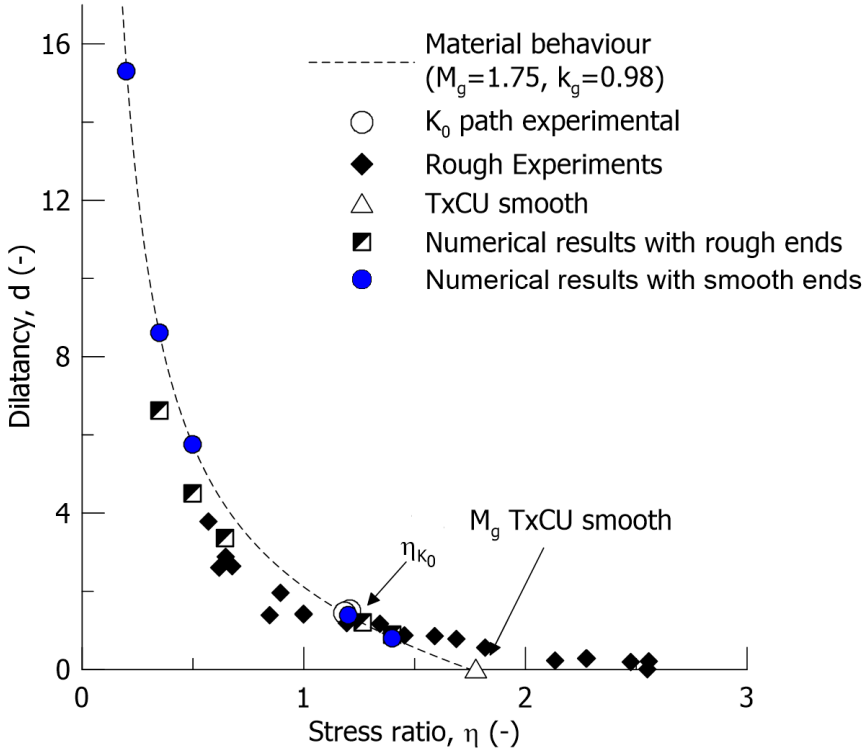

Figure 3.9: Stress-dilatancy relationship d - η for numerical and experimental results compared to the input non associated MCc law

3.6 Conclusions

In this Chapter the methodology, with which the numerical triaxial tests are performed and elaborated, is presented. The methodology includes the mesh of the finite element model, the parameters of the tested material as well as the global measurement of strains and stresses. After this, the validation of the finite element model is carried out against a benchmark TxCU test. Finally, the effects of end restraints on the pre-failure behavior of peat are investigated through means of stress dilatancy relationships. The stress dilatancy of rough tests obtained by the elaboration with global measurements differs from the material flow rule. More specifically, the numerical results for radial paths below K_0 underpredicts the dilatancy, while the opposite is observed for radial paths above K_0. It was shown that by using a classical MCc model the pre-failure response of peats cannot be captured. However, with using the friction angle obtained from a smooth TxCU test and using the Jacky's formula, a material flow rule fitted to "true" K_0 value can capture more than satisfactory the dilatancy of rough radial tests below K_0. For radial paths above K_0, higher dilatancy is observed experimentally than in the numerical simulation, and the necessity, from a modelling point of view, of adding the deviatoric hardening in the constitutive model is, afterwards, highlighted.

Chapter 4

Introduction of a volumetric and distortional hardening law in critical state model

4.1 Introduction

The aim of this chapter is to investigate at element level the influence of a volumetric and distortional hardening law on the mechanical response of MCc on undrained and drained triaxial tests for a high compressible soil as the peat investigated in Chapter 3. In Chapter 3, the experimental results show the possibility for the tested peat to sustain stress ratio at failure higher than the CSL. From a modelling point of view, this can be obtained by introducing a mixed volumetric and distortional hardening law.

4.2 Deviatoric Hardening

Instead of the traditional hardening law implemented in MCc model, the following combined hardening law is used.

$$dp'_0 = \frac{vp'_0}{\lambda - \kappa}(d\varepsilon_p^p + Dd\varepsilon_q^p) \tag{4.1}$$

The D is a parameter which controls the amount of contribution of plastic deviatoric strain increment $d\varepsilon_q^p$ in the evolution of the preconsolidation pressure p'_0 (i.e. hardening variable). It has been shown in Chapter 2 (see Eq. (2.46)) that the inclusion of deviatoric plastic strains in the formulation of hardening law results in non-null dilatancy at failure. However, if the coefficient D is assumed to be constant, the model response predicts a steady increase in the shear strength for the material with a stress path diverging from the CSL. One way of avoiding this problem is to assume that D can be a function of cumulative plastic deviatoric strains (Wilde, 1977). More particularly, it may decrease exponentially with the increase of plastic deviatoric strains.

$$D = D_0 e^{-D_1 \varepsilon_q^p} \tag{4.2}$$

so as at failure where the plastic shear strains are maximized ($D \to 0$) the stress ratio to be equal with M_g.

The D_0 and D_1 parameters indicate the initial value of D and the decrease rate related with the cumulative plastic deviatoric strains respectively. Considering undrained conditions, their

values can be calibrated by the parameter α which links the change of deviator stress with the change of mean effective stress (see Figure 2.3):

$$\alpha = -\frac{dp'}{dq} \tag{4.3}$$

The influence of D_1 on the decrease of D is visualised in Figure 4.1, where the higher the D_1 the faster the deviatoric plastic strains stop to contribute to the evolution of the yield surface and the conditions of Critical State are met.

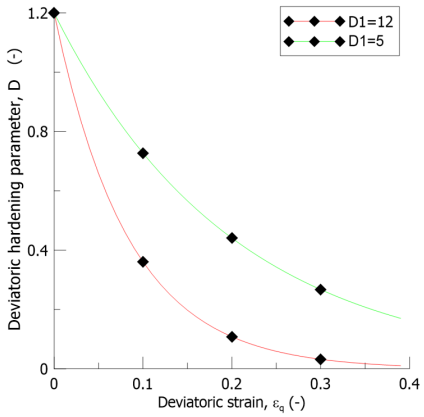

Figure 4.1: Influence of D_1 on the reduction of D with respect to deviatoric strain ϵ_q

4.3 Investigation of the model

In this Section, the effect of the mixed hardening on the mechanical response of a Normally Consolidated highly compressible peat during undrained and drained tests is examined in a single element test. First, the effect of having constant D and afterwards, the effect of a decaying D through an exponential law is investigated.

4.3.1 Undrained Tests

Constant D

Figure 4.2 shows the stress path in $p' - q$ space, along with the evolution of the two components of the mechanical behavior, the deviatoric stress q and pore water pressure u_w. For better understanding and further insight on the model, the α parameter which is related to the inclination of the stress path is also plotted.

Eq. (2.47) indicates that as D increases the stress obliquity at failure increases too. This can be verified by the plots of deviatoric stress q and of stress paths. In Figure 4.2a the stress paths are curved to the right for non null values of D. It is well known that the effective stress path in undrained conditions is linked with the evolution of pore pressure. Including the deviatoric plastic strains in the hardening law implies a transition between a contractive response to a dilatant response as it can be observed on the pore pressure response which firstly increases and then decreases. This behavior also is displayed to the plot of parameter α, where at $\eta = M_g = 1.75$, α is nullified implying that the curvature of the stress path also changes. Note that for $D = 0$ the model gives the same response as the MCc model with a traditional volumetric hardening.

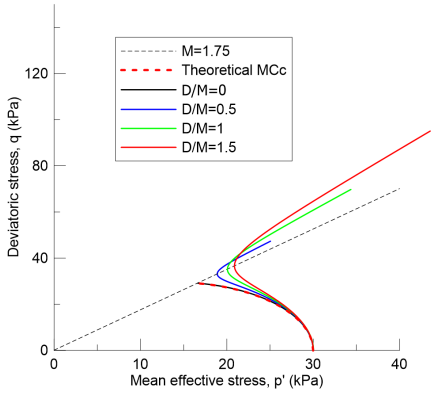

(a) Stress path in $p' - q$ space

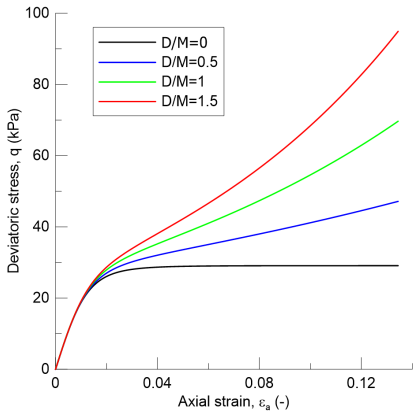

(b) Deviatoric stress q versus axial strain ε_a

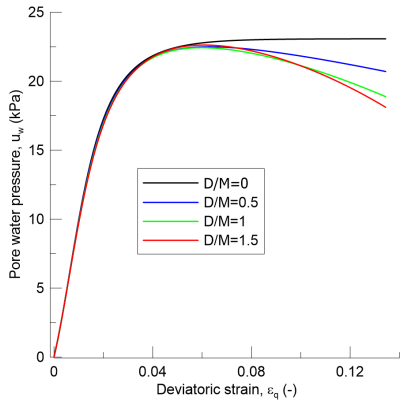

(c) Pore water pressures u_w versus deviatoric strain ε_q

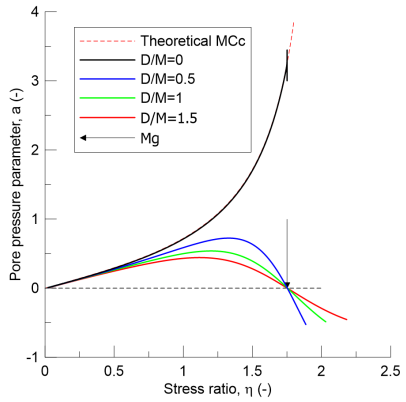

(d) Pore pressure parameter α versus stress ratio η

Figure 4.2: Undrained tests for various values of D

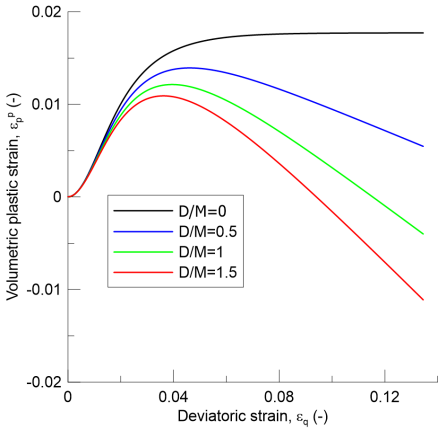

(a) Plastic volumetric strain ε_p^p versus deviatoric strain ε_q

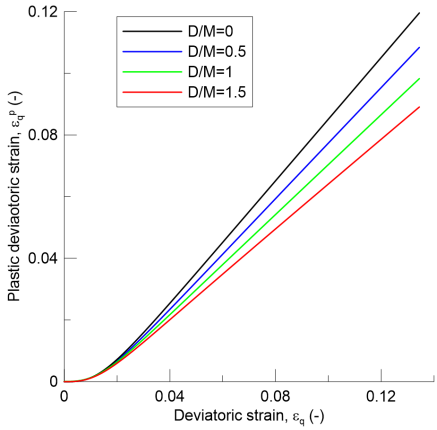

(b) Plastic deviatoric strain ε_q^p versus deviatoric strain ε_q

Figure 4.3: Evolution of plastic strains in undrained tests for various values of D

For better understanding of the model, Figure 4.3 depicts the development of plastic volumetric and deviatoric strains versus total deviatoric strains for various values of D. Under undrained conditions the following equations apply and they are useful to be mentioned:

$$d\varepsilon_p^p = -d\varepsilon_p^e = -\frac{dp'}{K} \tag{4.4}$$

$$d\varepsilon_q^p = d\varepsilon_q - d\varepsilon_q^e = d\varepsilon_q - \frac{dq}{G} \tag{4.5}$$

For $D = 0$ the behavior is contractive and reaches at critical state where no plastic volumetric deformation occurs as the MCc predicts. However, as the D increases, the dp' is not anymore monotonic which results to an initial contraction while there is reduction of mean effective stress p' and to dilation as the increment of mean effective stress increases. The dilation is more intense as the contribution of plastic deviatoric strains in the hardening law becomes more significant because the increase of p' is more profound for larger values of D.

With respect to plastic deviatoric strains, one should mention that the elastic deviatoric strains ε_q^e increase for larger increments of deviatoric stress q assuming a stable response with positive increment of q ($dq > 0$). Based on Eq. (4.5), this results to lower plastic deviatoric strains. Hence, the increase of D reduces the plastic deviatoric strains compared to the traditional MCc model for the same amount of strain.

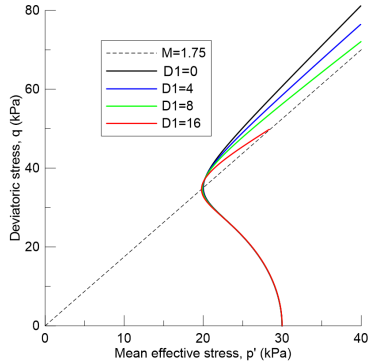

(a) Stress path in $p' - q$ space

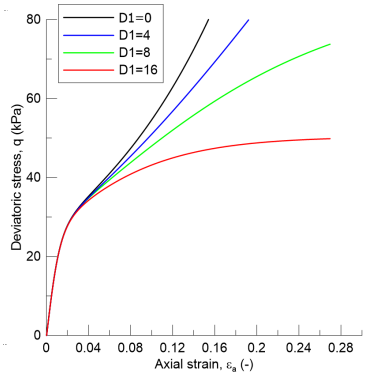

(b) Deviatoric stress q versus axial strain ε_a

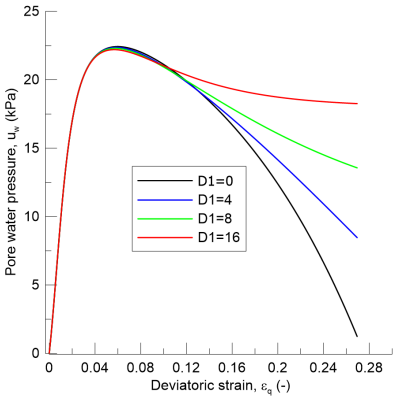

(c) Pore water pressures u_w versus deviatoric strain ε_q

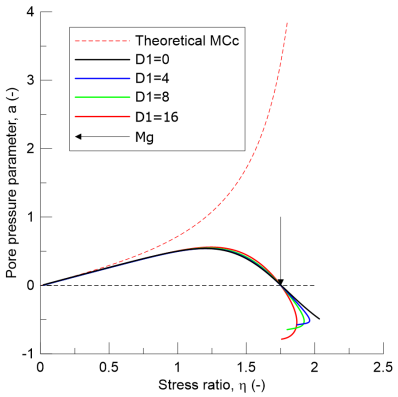

(d) Pore pressure parameter α versus stress ratio η

Figure 4.4: Undrained tests for various values of D_1

Decaying D

The adoption of a constant D introduces in the model response a fictitious infinite shear strength with a stress path overpassing the critical state line and steadily diverging from it. As a result a steady strain hardening behavior is obtained. However, it is desirable to have a material response which for large strain converge towards critical state again, thus, not showing a steady increase in the shear strength. By introducing an exponential decay to D, critical states can be achieved. This is observed in Figure 4.4, where for larger values of D_1 the stress path returns back to the critical state line more rapidly. This is indicated also in Figure 4.4d, where the α finally bends towards lower stress ratios. With respect to deviatoric stress and pore water pressures, the increase of D_1 clearly leads to the residual values of q and u_w, indicating that critical state conditions have been met. Especially for the pore water pressures, after the peak, observed already with constant D, the softening of pore pressures (e.g dilation) is not infinite and the asymptotic value is reached showing that no volumetric deformation occurs (Critical State).

4.3.2 Drained Tests

Up to here, the model was tested under undrained triaxial conditions, and the results can be justified. Herein, the influence of deviatoric hardening in the drained tests is examined.

Due to the high compressibility of the tested material, it is difficult to bring it to failure under drained conditions. More specifically, Figure 4.5 presents a drained compression test for a high compressible material simulated with MCc. It is observed that failure has not been achieved even for strains approximately equal to 60%. The above consideration has been reported also by Zhang and O'Kelly (2014), where the authors mention that deviatoric stress continued to increase approximately linearly with axial strain even for a peat specimen without fibers. Given the above considerations, it was selected to reduce the compressibility of the soil in order to test the deviatoric hardening under drained conditions in a MCc model.

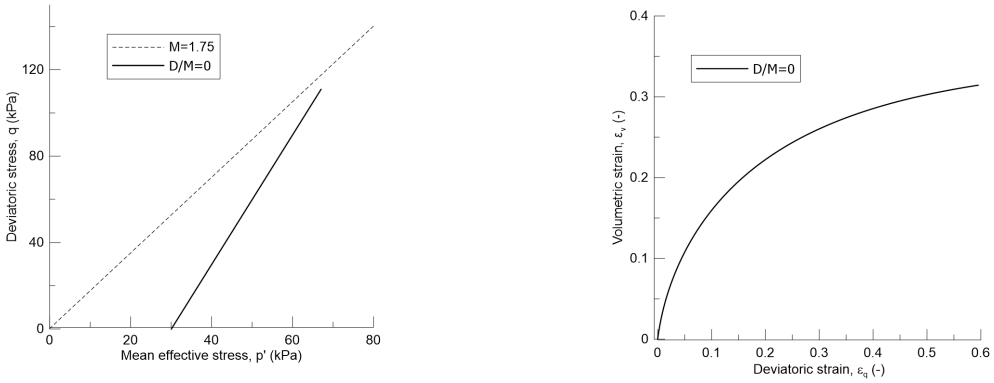

(a) Stress path in $p' - q$ space

(b) Volumetric strain ε versus deviatoric strain ε_q

Figure 4.5: Drained test with MCc model for a highly compressible material

Figure 4.6 presents the response in drained conditions for $D = 0$, $D = 0.35$, $D_0 = 0.35, D_1 = 3$ and $D_0 = 0.35, D_1 = 9$. With using a constant non-null value of D the stress path overpasses the Critical State Line (CSL), having a continuous increase of deviatoric stress q, resulting to a ficticious predicted strength. In terms of volumetric response, typical dilative behavior is observed. While decaying of D is considered, the stress path overpassing of CSL is reduced for higher values of D_1. Looking at deviatoric stress q response, with increasing values of D_1, a

diminishing peak is observed followed by a softening behavior until the critical state is reached. In terms of volumetric strain, the increase of D_1 results into a reduction in the predicted dilation, and critical state conditions are met for lower values of strain.

It has been noted that the inclusion of deviatoric plastic strains in the hardening law has the same qualitative effect on drained and undrained tests, leading to higher stress obliquity than M_g and to dilative behavior. When the contribution of the deviatoric plastic strains is dependent on the strain level critical state conditions can be achieved, eliminating the disadvantage of continuous dilation observed with a constant value of D. However, a difference between the drained and undrained tests arises and it is related to the amount of plastic deviatoric strains exhibited in each test conditions. Looking at Figures 4.6d and 4.3b, it is seen that in undrained condition the generated deviatoric strains are lower for the same amount of strain.

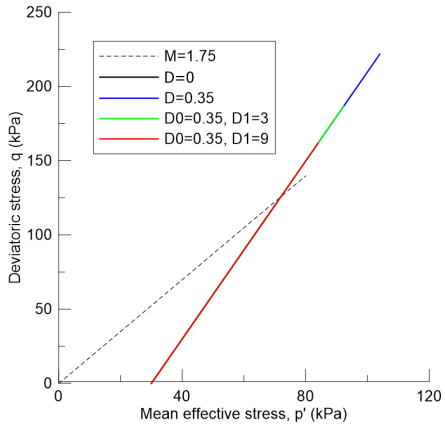

(a) Stress path in $p' - q$ space

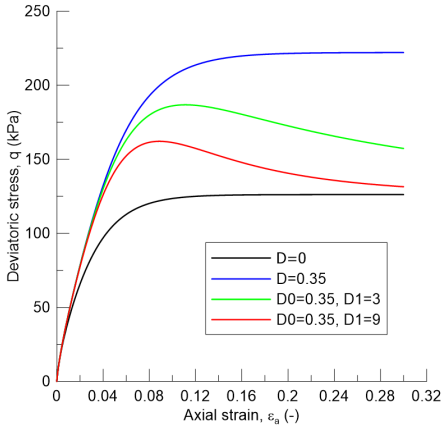

(b) Deviatoric stress q versus axial strain ε_a

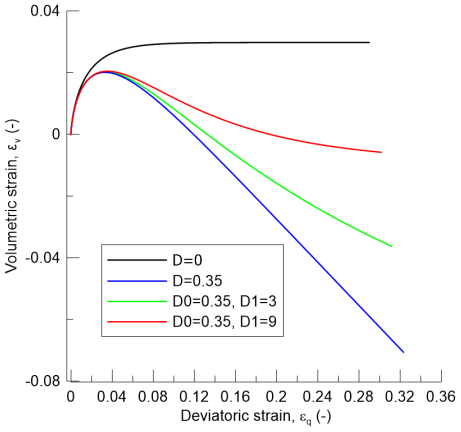

(c) Volumetric strain ε_v versus deviatoric strain ε_q

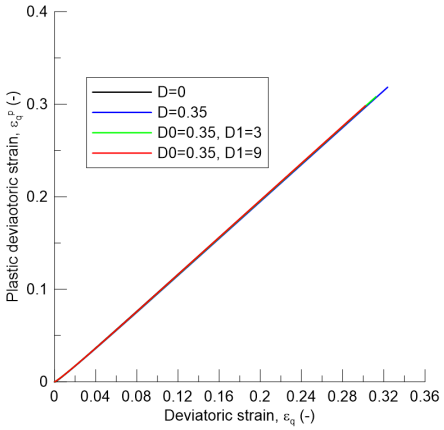

(d) Plastic deviatoric strain ε_q^p versus deviatoric strain ε_q

Figure 4.6: Drained tests for constant and decaying D

4.3.3 Conclusions

In summary, an extension of MCc has been presented by assuming that deviatoric plastic strains also contribute to the hardening process. Two parameters are introduced D_0 and D_1. By setting $D_0 = 0$, the MCc model is retrieved.

It has been found that the deviatoric contribution to the soil hardening change profoundly the performance of the new model. In particular, higher stress obliquity and continuous dilation is observed for higher values of D_0. By keeping the D_1 null, the critical state is not reached, because the size of yield surface is dependent on both the plastic volumetric and deviatoric strain increments, and the latter is not zero at critical state. By increasing the D_1, critical state is asymptotically reached.

Chapter 5

Main FEM Analyses

5.1 Introduction

The new model has been implemented into the finite element programme LAGAMINE in order to simulate boundary value problems. The model formulation along with the implementation is first described in this Chapter and, afterwards, the model performance is discussed.

5.2 Model description in LAGAMINE

5.2.1 Formulation

Analytical description of the model has been given in Chapter 2. Herein, a brief summary of the 4 ingredients of the model, based on MCc framework, is given.

Elasticity

In the elastic domain non-linear elasticity is used:

$$d\sigma' = \mathbf{D} d\varepsilon \tag{5.1}$$

where $\mathbf{D}$ is given by Eq. (2.2), and K and G by Eq. (2.19) and (2.20) respectively.

Yield surface

Generalized shapes of yield surface adopted by McDowell and Hau (2004) are used in this model:

$$q^2 = -\frac{M_f^2}{1-k_f}\left(\frac{p'}{p'_0}\right)^{\frac{2}{k_f}} p_0'^2 + \frac{M_f^2 p'^2}{1-k_f} \tag{5.2}$$

where M_f intersect the yield locus at the apex, k_f controls the shape of the yield surface, p_0 is the preconsolidation pressure controlling the size of yield surface. In addition, there is the option of extending the model to 3D stress state by introducing the M_f to be dependent on the Lode angle through Van Eekelen equation, as it is described in Chapter 2.

Flow rule

The flow rule in this model is given by:

$$\frac{d\varepsilon_p^p}{d\varepsilon_q^p} = \frac{M_g^2 - \eta^2}{k_g \eta} \tag{5.3}$$

where k_g controls the shape of the plastic potential (see Chapter 2). For $k_g = 2$ the MCc plastic potential is retrieved.

Hardening law

The hardening law is a mixed hardening law, already described in previous Chapter.

5.2.2 Implementation

The integration of constitutive equations is based on the cutting plane algorithm, proposed by Ortiz and Simo (1986) and modified by Dieudonné (2016). Two consecutive steps are involved in this procedure:

- The stress path is assumed to be elastic and an elastic predictor σ_e is computed. The yield criterion is evaluated at this state. If the stress lies inside the elastic domain, the final state is elastic and equal to the trial stress.
- If the elastic trial stress is violating the yield criterion, a plastic return mapping, called plastic corrector is computed to return the stress state onto the yield surface. In the cutting plane algorithm, an iterative procedure is used to restore the consistency of the mechanical state. At each iteration, the incremental constitutive equations are integrated using an explicit forward Euler scheme.

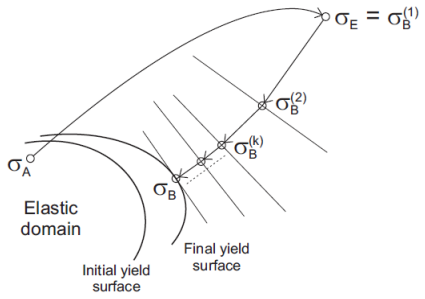

Figure 5.1: Geometric interpretation of the cutting plane algorithm for the case of associative plasticity (retrieved by Dieudonné (2016))

More specifically, the LAGAMINE gives as input the total strain field in the integration routine. Based on this strain increment $d\varepsilon$ the elastic predictor σ_e is found:

$$\sigma_e^{(k+1)} = \sigma_A^{(k)} + \mathbf{D}d\varepsilon \tag{5.4}$$

If the yield criterion is violated, the cutting plane algorithm with forward substepping determines the up-dated stress state σ_B as:

$$\sigma_B^{(k+1)} = \sigma_B^k + d\sigma^{p(k+1)} \tag{5.5}$$

where $d\sigma^{p(k+1)}$ is the plastic stress increment. The first elastic predictor is used as starting point of the iterative process. The plastic stress increment is computed according to:

$$d\sigma^{p(k+1)} = -\mathbf{D}(\sigma_B^k)d\varepsilon^{p(k+1)} \tag{5.6}$$

where $d\varepsilon^{p(k+1)}$ is the plastic strain increment at iteration $k+1$, whose value is given by:

$$d\varepsilon^{p(k+1)} = d\lambda \frac{\partial g}{\partial \sigma_e^{(k+1)}} \tag{5.7}$$

with $d\lambda$, the plastic multiplier increment and g the flow surface related to the yield surface f. At every iteration, the yield criterion f is linearised around the current values of trial stresses and state variables, in order to compute the plastic multiplier increment:

$$f_B^{(k+1)} = f(\sigma_e^{(k+1)} + d\sigma^{p(k+1)}, \kappa_e^{(k+1)} + d\kappa^{(k+1)}) \tag{5.8}$$

$$= f(\sigma_e^{(k+1)}, \kappa_e^{(k+1)}) + \frac{\partial f}{\partial \sigma_e^{(k+1)}} d\sigma^{p(k+1)} + \frac{\partial f}{\partial \kappa_e^{(k+1)}} d\kappa^{(k+1)} \tag{5.9}$$

with

$$d\kappa^{(k+1)} = \frac{d\kappa}{d\varepsilon^{p(k+1)}} d\varepsilon^{p(k+1)} = d\lambda \frac{d\kappa}{d\varepsilon^{p(k+1)}} \frac{dg}{d\sigma_e^{(k+1)}} \tag{5.10}$$

Finally, by dictating the consistency equation $f_B^{(k+1)}$ and using Eq. (5.6), the increment of plastic multiplier is calculated:

$$d\lambda = \frac{f(\sigma_e^{(k+1)}, \kappa_e^{(k+1)})}{\frac{\partial f}{\partial \sigma_e^{(k+1)}} \cdot \mathbf{D} \cdot \frac{\partial g}{\partial \sigma_e^{(k)}} - \frac{\partial f}{\partial \kappa_e^{(k+1)}} \frac{d\kappa}{d\varepsilon^{p(k+1)}} \frac{\partial g}{\partial \sigma_e^{(k+1)}}} \tag{5.11}$$

5.3 Verification

The verification of the implemented model in Lagamine is done in this Section with respect to the Single Element Code. The capabilities of the new implemented model are firstly verified for undrained and drained triaxial compression tests with respect to the single element code used in Chapter 4. The Single Element Code uses the explicit Runge-Kutta-Dormand-Prince scheme proposed by Sloan et al. (2001), while the code inside LAGAMINE is an implicit algorithm with explicit sub-stepping at the level of the constitutive model.

In Figure 5.2, the comparison between the two codes for different values of deviatoric hardening parameters is presented. It is observed that the responses of the two codes perfectly match.

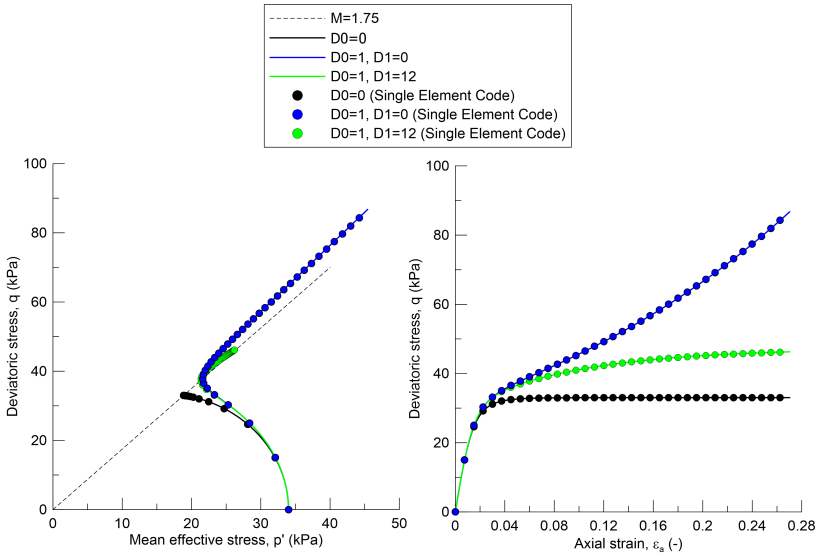

Figure 5.2: Undrained stress path and deviatoric stress vs strain with deviatoric hardening between LAGAMINE and Single Element Code

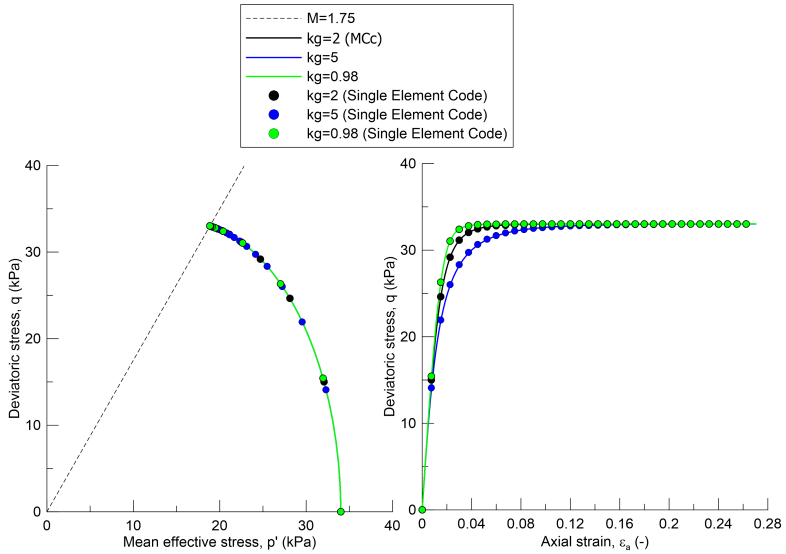

Figure 5.3: Undrained stress path and deviatoric stress vs strain for different flow rules between LAGAMINE and Single Element Code

Figure 5.3 depicts the response of the two codes for a MCc model (only volumetric hardening) with different implemented flow rules. The results from the two codes are in good agreement. Explaining the deviatoric strain response, it is useful to refer to Figure 2.2a, where different shapes of plastic potential surfaces are plotted. When the plastic potential surface is skewed to the right (small k_g), the direction of the plastic strains in an undrained stress path of a normally consolidated material is orientated towards the plastic volumetric strains, so the plastic volumetric strains evolve more quickly. As a result the hardening of the yield surface is more intense and higher stress ratios are achieved. Hence, the response is stiffer for lower values of k_g.

In addition, the stress paths of Figure 5.3 are identical, despite the different used flow rules. This is justified by the fact that plastic and elastic volumetric strains in an undrained path are canceled out which forces a link between changes in mean effective stress p' and preconsolidation pressure p'_0 controlling the size of the yield surface (Muir Wood, 1990). Thus, the geometry of the yield surface in an undrained path determines the stress path, and not the shape of the flow rule.

5.4 Calibration of the Model

The proposed model has in total 10 parameters. These are the initial void ratio e, the slope of the isotropic normal compression line λ, the slope of the isotropic unloading and reloading line κ, the Poisson's ratio ν', the M_f, M_g, k_f, k_g and the hardening parameters D_0 and D_1. The first 4 are easily obtained and they are the same for every critical state model. If the maximum flexibility provided by the equations of yield surface and plastic potential is desired, one can choose different values for M_f and M_g. If associated plasticity is demanded, then $M_f = M_g$ and $k_f = k_g$. However, an explanation for the general determination of the parameters is given below.

The parameters M_f, M_g, k_f and k_g can be determined by conventional drained tests (McDowell and Hau, 2004). By performing multiple radial stress paths, the yield points along these stress paths can be found. Then, the stress ratio M_f corresponding to the peak value of p/p'_0 can be found, and a suitable value of k_f can be determined. This is depicted in Figure 5.4.

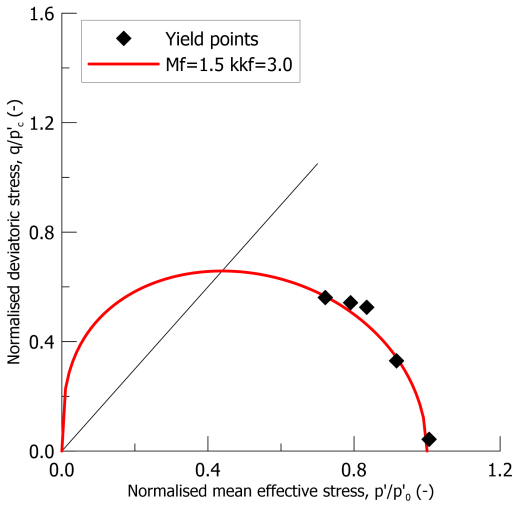

Figure 5.4: Determination of yield surface parameters M_f and k_f

The way of determination of the parameters of plastic potential has been discussed in Chapter 3. By performing smooth TxCU tests the friction angle can be obtained which is related to M_g, and by using the Jacky's formula, a value for k_g can be selected in order a "true" K_0 value to be predicted. However, the selection of k_g is not only based on the correct estimation of K_0, but also on the fitting of the diagram of plastic strain increment vector versus stress ratio (Figure 5.5).

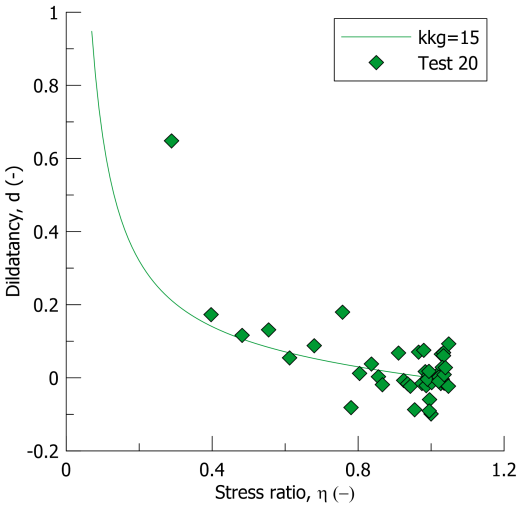

Figure 5.5: Determination of plastic potential parameter k_g

As far as the deviatoric hardening parameters are concerned, their determination is not so straightforward. In order to propose a way of calibrating these parameters, a reflection on basic equations should be done. In an undrained test, the elastic and plastic volumetric strain are canceled out and by using Eq. (2.18) and (2.38a), it is retrieved that:

$$\kappa \frac{dp'}{vp'} = -\frac{\lambda - \kappa}{vp'_0} \tag{5.12}$$

Rewriting the mixed hardening law in terms of $d\varepsilon_p^p$ and using Eq. (5.12) it yields:

$$d\varepsilon_p^p = \frac{\lambda - \kappa}{v} \frac{dp'_0}{p'_0} - Dd\varepsilon_q^p \tag{5.13}$$

$$\kappa \frac{dp'}{p'} = -(\lambda - \kappa) \frac{dp'_0}{p'_0} + vDd\varepsilon_q^p \tag{5.14}$$

Recalling that the slope of undrained path is given by $\alpha = -\frac{dp'}{dq}$ the Eq. (5.14) becomes:

$$\alpha \frac{dq}{p'} = \frac{\lambda - \kappa}{\kappa} \frac{dp'_0}{p'_0} - \frac{vD}{\kappa} d\varepsilon_q^p \tag{5.15}$$

Regarding the latter equation, the first and second part of the right-hand side of equation are always positive as expansion of yield function occurs and positive deviatoric strains develop during contraction. A stable deviatoric response is also considered, so $dq > 0$. Consequently, in the contraction domain, α firstly increases due to the initially minimal deviatoric strains and then decreases due to the deviatoric hardening component. The ratio $\frac{D}{\kappa}$ controls the decrease of α. By fitting single element analyses to the experimental values of α a combination of parameters D_0 and D_1 can be found.

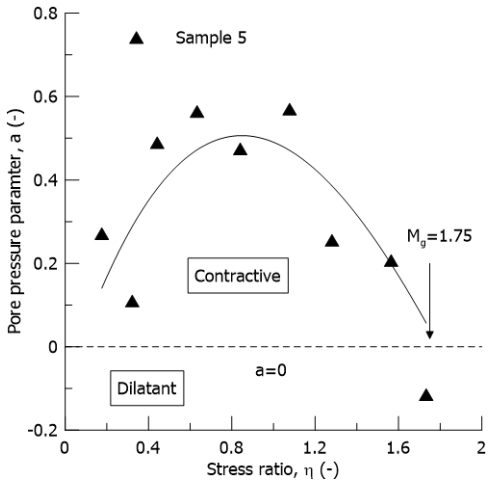

Figure 5.6: Visualization of determining of hardening parameters D_0 and D_1

5.5 TxCU tests

As demonstrated in Chapter 3, end restraints affect the observed behaviour from standard triaxial tests with rough end platens, so the single element analyses from Chapter 4 are not able to fully capture the observed soil response. Herein, TxCU tests are simulated as a boundary value problem in order to take into account the effects induced by the presence of rough platens.

The Table 5.1 presents the TxCU tests done experimentally, the corresponding numerical tests, as well as the height to diameter ratio, initial and boundary conditions of each test. There are in total 5 tests, 4 with rough end platens and 1 with smooth end platens. The height to diameter ratio ranges from 1.5 to 3 for P1-P4 and for P5 it is equal to 1.5, test in which end restraint is minimized and the true material behavior can be revealed without any boundary effect. It should be noted that the tests with the lower height to diameter ratio and rough boundaries are predominantly influenced by the end restraints. In addition, the strain rate was kept constant in order to replicate the experimental data by varying the displacement rate of each Test. Finally, the isotropic consolidation on which they specimens were subjected was not modelled in this Thesis.

Table 5.1: TxCU Tests

Test	Numerical	H0/D0	Boundary	$p'_0(kPa)$	e_0	OCR	Strain rate
15	P1	1.5	Rough	34	7.5	1	0.02%
16	P2	2.0	Rough	34	7.5	1	0.02%
17	P3	2.5	Rough	34	7.5	1	0.02%
18	P4	3.0	Rough	34	7.5	1	0.02%
20	P5	1.5	Smooth	34	7.5	1	0.02%

Before proceeding, a sensitivity analysis on the time step size has been performed. Figure 5.7 presents the obtained stress path and deviatoric stress strain response for 3 different time steps. It is shown that for $dt = 270s$ there is no significant deviation with the previous time step size. Thus, $dt = 270s$ is used as time step in the analyses of this Chapter. Concerning the mesh discretization, the same discretization as in Chapter 3 is considered.

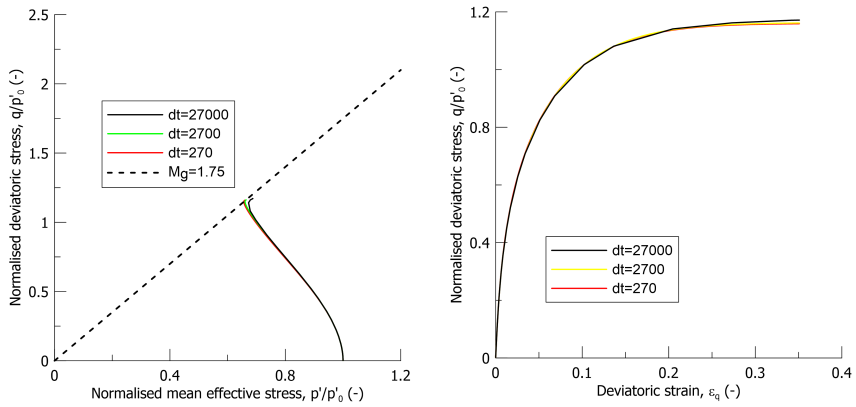

Figure 5.7: Sensitivity analysis on the time step size

5.5.1 Calibrated parameters from the smooth test

This series of analyses aims to examine whether with the calibrated parameters from the smooth test it is possible to capture the response of rough tests by simulating them as boundary value problems. The Table 5.3 presents the set of parameters for each analysis. The critical stress ratio $M_g = 1.75$ corresponds to a friction angle of $\phi' = 42.6°$, the obtained friction angle at failure for the smooth case. In addition, the yield locus parameters, the other plastic potential parameter and the hardening parameters remain the same for all the test conditions. The compressibility index, the unloading reloading compression index and the poisson ratio remain constant throughout the Thesis.

Table 5.2: Parameters of tested material based on Test 20

λ	κ	ν'	M_f	k_f	M_g	k_g	D_0	D_1	$k(m/s)$
2	0.3	0.2	1.5	3	1.75	15	1.2	12	10^{-9}

In Figure 5.19, the normalised stress paths by p'_0 which is the mean effective stress at the beginning of shear, the excess pore pressure development with the deviatoric strain and stress-strain development of numerical simulations are presented in comparison with the corresponding experimental curves. It should be noted that the presented numerical results are obtained with correcting stresses with the average diameter between the diameter of the nominal area and of the equivalent cylinder as demonstrated in Chapter 3.

It is clearly observed that the P5 test is in a good agreement with its corresponding experimental

test for all the diagrams, as it was expected. For the rough tests, concerning the stress path, there is an obvious distinction between the P1-P4 tests and the P5 test, but there is, clearly, a divergence with the experimental results. Only for the P4 test one can say that it is in well agreement with Test 18, as due to its large height to diameter ratio the end restraints effects are minimized and this test can resemble to a smooth test.

In order to have a further insight to the stress paths, the diagrams of excess pore pressures and of deviatoric stress are presented. It is seen that the numerical code can capture the initial experimental response of the pore pressure and of the deviatoric stress. However, the final portion of both the excess pore pressure and deviatoric stress deviates from the experimental observations. Though, the constrained lateral displacement of top and bottom end platens leads to higher excess pore pressures and deviatoric stress. Only the former is captured numerically, as the excess pore pressures of the rough tests are overpredicted in comparison with those of the smooth test without someone can observe a distinct trend between the rough tests. The predicted deviatoric stress of the P1-P4 tests is not in good agreement with the experiments, as it is roughly the same with the one from the P5 test.

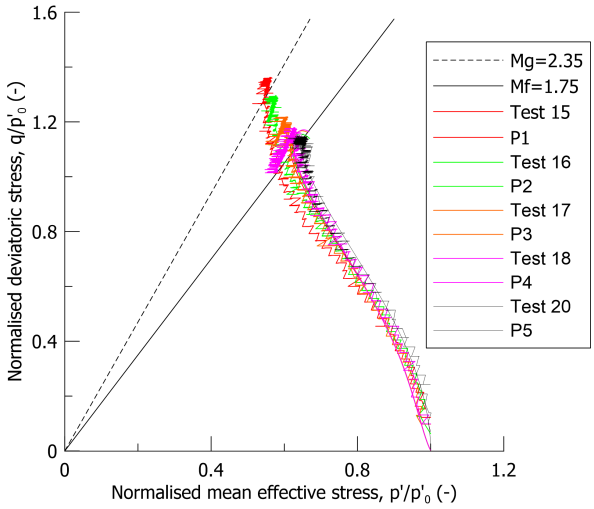

(a) Normalised effective stress path

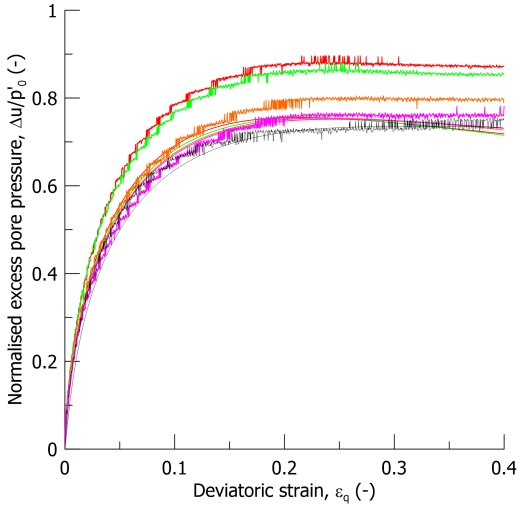

(b) Normalised excess pore pressure vs deviatoric strain

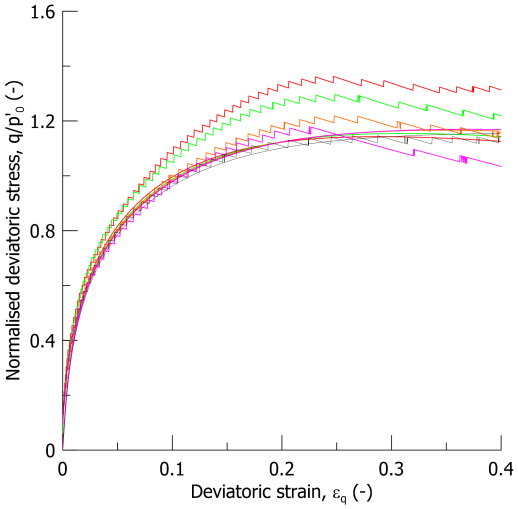

(c) Normalised deviatoric stress-strain

Figure 5.8: Results with parameters from smooth test calibration

To sum up, with this set of parameters, the numerical code can capture the difference between the rough tests and smooth test only in terms of excess pore pressure. However, the model is not capable to capture the influence of height to diameter ratio on both the deviatoric stress and excess pore pressure as these are observed experimentally.

5.5.2 Different parameters for each rough tests

Since using the same parameters from the smooth test P5 for all the tests was ineffective of capturing the experimental curves of tests affected by the end restraints, a possible solution would be to change the input parameters of Tests P1-P4. Since reaching to higher stress ratio with decreasing height to diameter ratio is demanded, the only changing parameters between the various tests could be the hardening parameter D_1 which controls the decrease of the contribution of the plastic deviatoric strains on the evolution of preconsolidation pressure or even D_0. However, herein, the intention is to replicate the material behaviour of samples with rough ends with the minimum changing of the parameters from the smooth test as much as possible. Hence, changing the friction angle for the rough tests is out of the scope of these analyses, because the friction angle of the material is an inherent material parameter and the higher observed friction angles in the laboratory conditions is due to the presence of end restraints. By changing D_1, it is implicitly considered that the boundary affects a model parameter, which constitutes a limitation of the model in its current stage. However, it seems that there could be a connection between end restraint effects and the dimensions of the fibers with the distortional hardening.

To give a better understanding on changing D_1, higher values of D_1 lead to a more rapid decrease of D and hence, to lower stress obliquity in critical state. Shorter tests are influenced more by end restraints, and the attempt to model the peat behavior with the distortional hardening should take into account the interaction between fibers and geometry of the sample. Consequently, this can be incorporated by using smaller values of D_1 in an intuitive, at this stage, manner. In addition, the D_1 is aimed to keep as much more closely to the reference value of smooth test. The Table 5.3 summarizes the input parameters of these analyses and Figure 5.9 shows the trend of D_1 with respect to the height to diameter ratio.

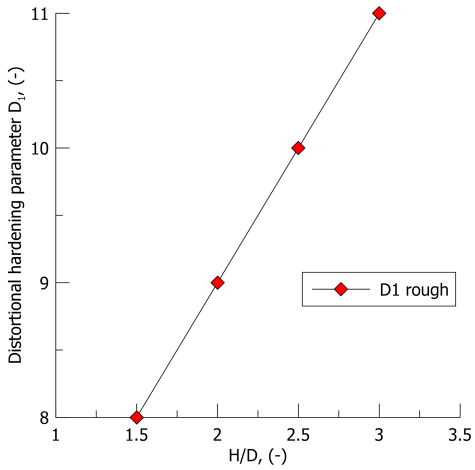

(a) D_1 correlation with the H/D of the specimens

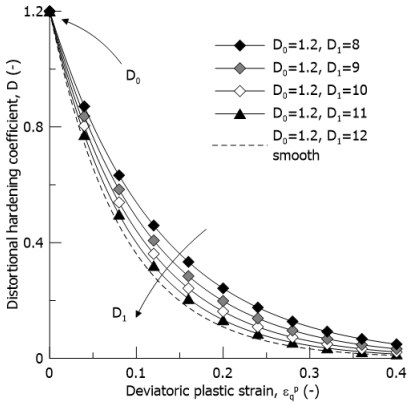

(b) Corresponding decay of the distortional hardening coefficient D with the cumulative deviatoric plastic strain ε_q^p

Figure 5.9: D_1 parameter for this set of analyses

Table 5.3: Parameters of tested material

Numerical Test	λ	κ	ν'	M_f	k_f	M_g	k_g	D_0	D_1	$k(m/s)$
P1	2	0.3	0.2	1.5	3	1.75	15	1.2	***8***	10^{-9}
P2	2	0.3	0.2	1.5	3	1.75	15	1.2	***9***	10^{-9}
P3	2	0.3	0.2	1.5	3	1.75	15	1.2	***10***	10^{-9}
P4	2	0.3	0.2	1.5	3	1.75	15	1.2	***11***	10^{-9}
P5	2	0.3	0.2	1.5	3	1.75	15	1.2	***12***	10^{-9}

By observing the stress paths of Figure 5.10a, there is now a clear distinction between the stress paths of the rough tests and the influence of height to diameter ratio on the numerical results is noticeable. As far as the convergence with the experimental data is concerned, the final part is not caught. This also can be seen by analysing the stress path into the volumetric part and the deviatoric part by Figure 5.10b and 5.10c respectively. The deviatoric part is well captured, while the volumetric part is captured initially, but there is a deviation on high strain levels. More specifically, the initial build up of pore pressures is in good agreement with the experimental data. Though, the peak values of pore pressures are caught only for the Tests P3 and P4. After this observed peak value, a softening behavior follows leading to lower values compared with the experimental results at the final state of the analyses. This softening behavior is not observed experimentally. Thus, based on these observations, the stress path deviation at high stress ratios is related with softening of pore water pressures at high strain levels.

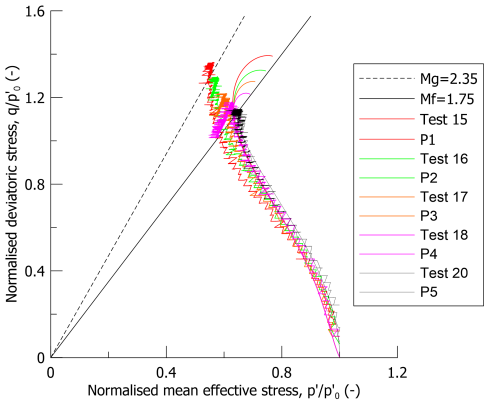

(a) Normalised effective stress path

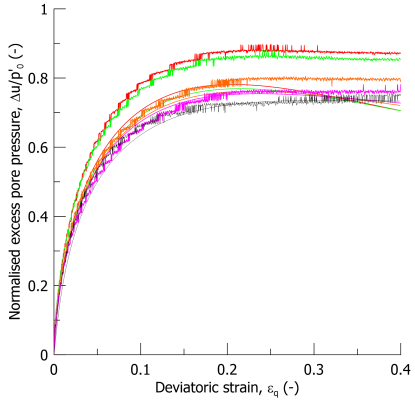

(b) Normalised excess pore pressure vs deviatoric strain

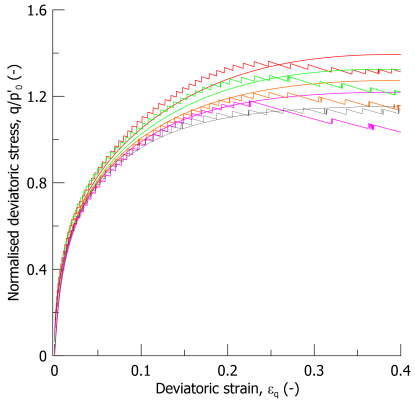

(c) Normalised deviatoric stress-strain

Figure 5.10: Results with D1 varying

5.5.3 Investigation on the effect of Lode angle

It is well known that experiments with rough end platens do not deform uniformly and the 3D stress state deviates from the axisymmetric points in the deviatoric plane (compression or extension points) due to the development of shear stress along the specimen. In Figure 5.12, the distribution of lode angle at the final state of the analysis is presented. It is seen that the central part of the soil is under compression and it carries the axial load, as the Lode angle is equal to 30°. The outer part dilates and then, the Lode angle decreases and deviates from the axisymmetric stress state.

The deviation from the axisymmetric stress state for some elements implies that the strength of the material is not the maximum. In addition, this reduction of stresses means that the material becomes less stiffer and more displacements are allowed. The above are verified in Figure 5.14, where smaller deviatoric stresses are predicted and lower pore pressures are observed as the larger lateral allowable expansion leads to larger potential dilation which results to a maximum potential pore pressure reduction.

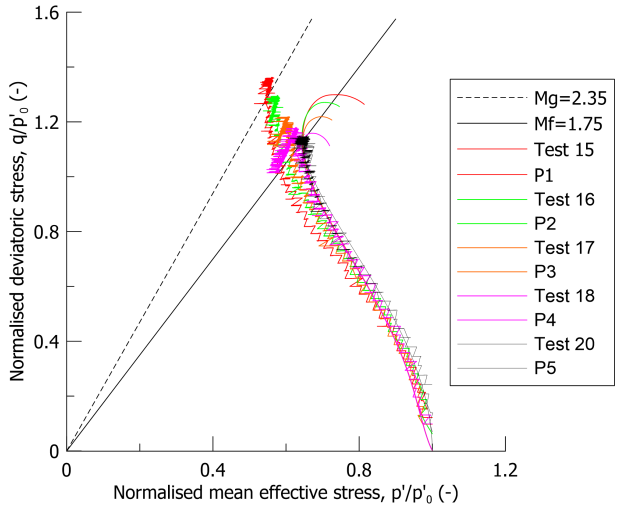

(a) Normalised effective stress path

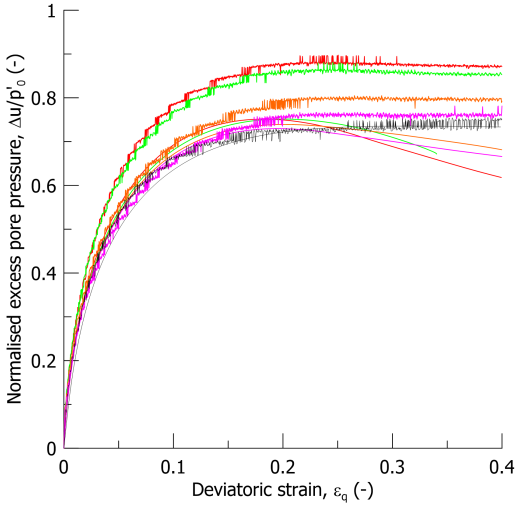

(b) Normalised excess pore pressure vs deviatoric strain

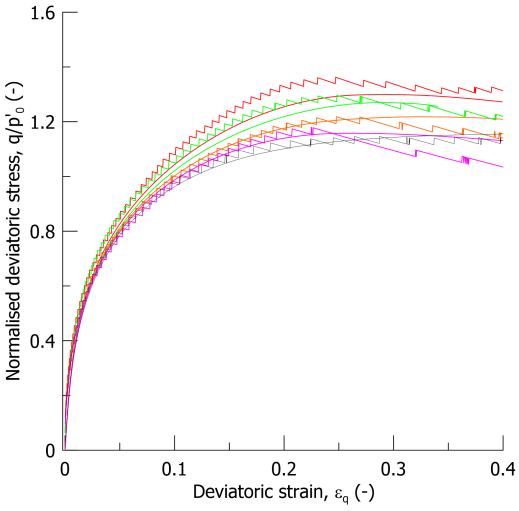

(c) Normalised deviatoric stress-strain

Figure 5.11: Results with Van Eekelen in deviatoric plane

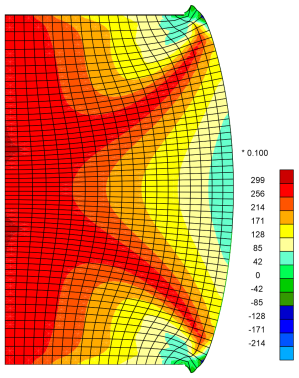

Figure 5.12: Lode angle distribution for P1 test (positive compression, negative extension)

5.5.4 Discussion

Herein, a discussion about the capabilities and limitations of the proposed model concerning the capturing of undrained behavior of peat under triaxial conditions with end restraint effects is done. The mechanical response of peat can be divided into the volumetric behavior and deviatoric behavior. The former has been proved that it can be captured in a satisfactory manner, while the latter can be only in some qualitative agreement with the experimental results. More specifically, with the suitable selection of parameters for the various rough tests, the deviatoric stress is reproduced well, while the pore pressure generation is underestimated for the shorter tests. In addition, a softening in the pore water measurements is observed which is not found in the experimental results.

In order to have a further insight on the developing mechanisms undergoing a TxCU test, the isolines of excess pore pressures for the Test P1 at 4 strain levels, which are shown in Figure 5.13, are depicted in Figure 5.14. By looking the distribution of excess pore pressures at 5% axial strain, the water is drained from bottom and top towards the mid where the pressures are lower. At higher strains, the pore pressures distribution stops to be horizontally stratified, and the isolines start to shift their direction, from horizontally to vertically. During this alternation, the outer elements start to dilate while the elements at the center start to compress. At the final state, the final deformation mode of a typical rough test can be depicted where bulging has been occurred. Then, the elements at the perimeter of the specimen dilate and the center elements carry the axial load.

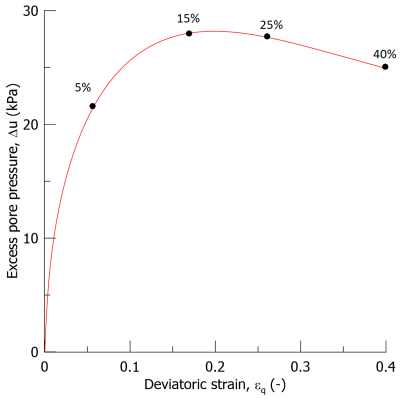

Figure 5.13: Development of excess pore pressure at bottom for P1 Test

The alternation of isolines direction is crucial for explaining the pore pressure softening. In more detail, the pore pressures in the mid, which are lower in general than in the edges, start to influence gradually the pore pressures at the boundaries as the axial strain increases. Hence, the pore pressures at bottom for higher strains decrease due to the radial expansion of middle part and the consequent pressure relief on this part of the specimen, which is transmitted to the boundaries.

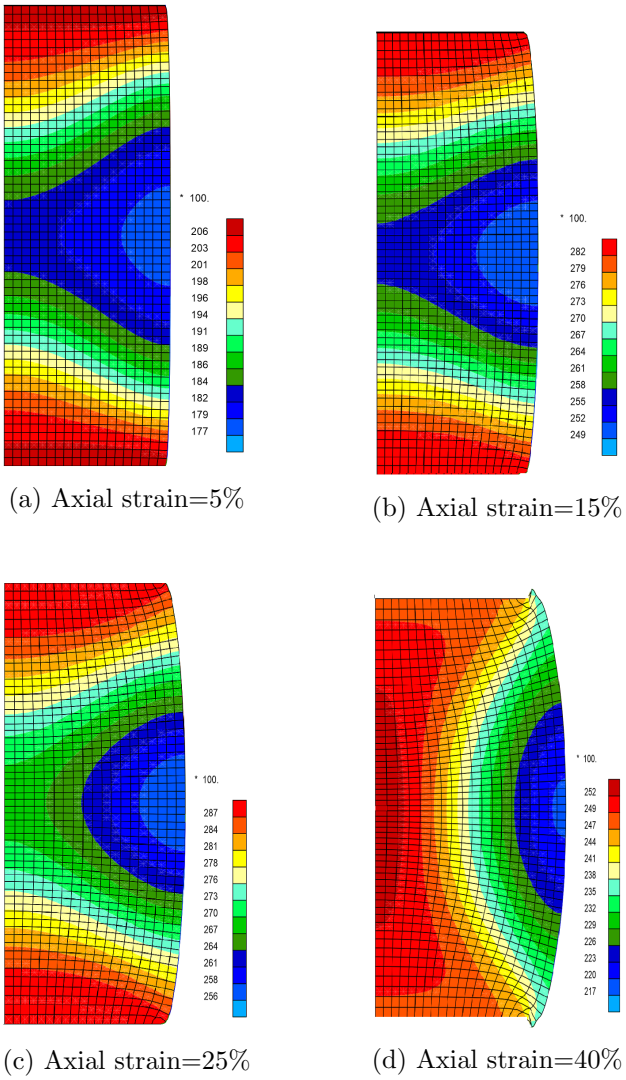

(a) Axial strain=5%

(b) Axial strain=15%

(c) Axial strain=25%

(d) Axial strain=40%

Figure 5.14: Isolines of excess pore pressures for different strain levels depicted at deformed mesh for Test P1 (absolute pressure in Pa)

This softening of pore pressures at high strains is immediately related with the deformation mode. Figure 5.15 shows schematically the formation of dead zones and the free failure zone between them for a tall and short test. In the short tests, the free failure zone is smaller in volume as the dead zones imposed by the end restraints play a more significant role. The above is also depicted in Figure 5.16 where the excess pore pressures for Test P1-P4 are presented. The dead zones of Tests P1 and P2 are more profound than of Tests P3 and P4 and the gradient of pore pressures at the central part of the specimen is intense in the radial direction in contrast with the Tests P3 and P4 where a more uniform distribution at the central part along the radial direction is observed. Thus, the softening of pore pressures is more intense in these tests, because the pore pressures at mid are transferred more rapidly at the boundaries due to the influence of the boundaries at the central part of the specimens.

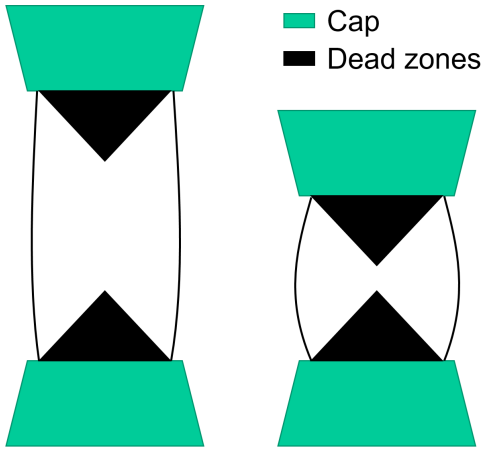

Figure 5.15: Schematic formation of dead zones inside a tall and a short specimen

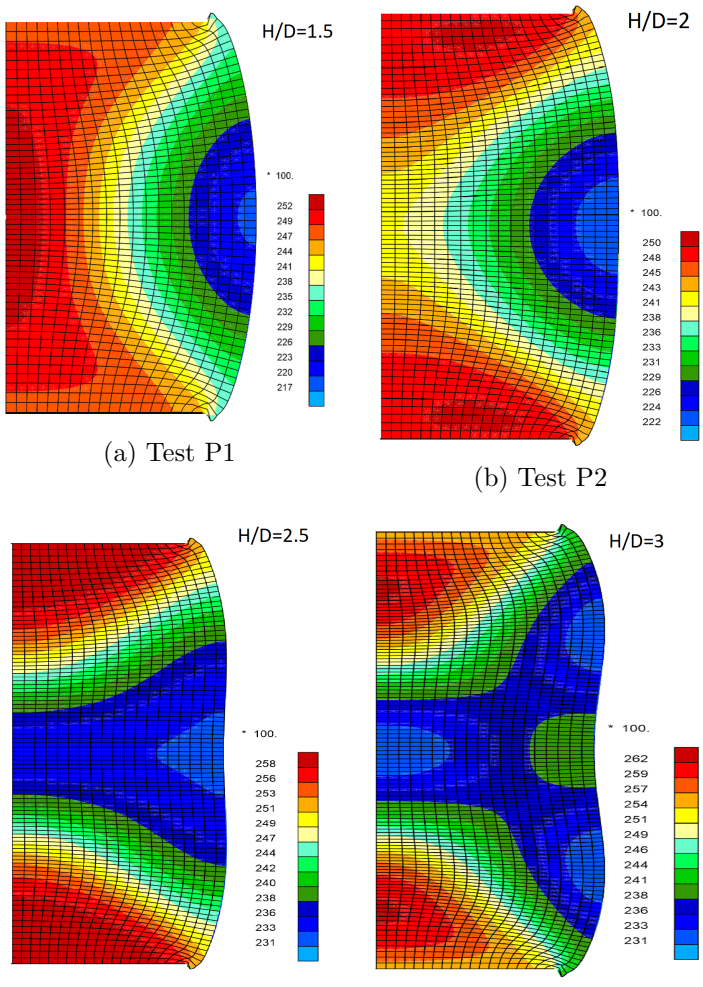

(a) Test P1

(b) Test P2

(c) Test P3

(d) Test P4

Figure 5.16: Isolines of excess pore pressures at final state depicted at deformed mesh for different rough tests (absolute pressure in Pa)

Investigation on the effect of permeability

The permeability and void ratio have been determined in the lab with an oedometer apparatus, equipped with a pore pressure transducer. The void ratio attained by the samples during shear ranged between 6.5 and 7.5, and the corresponding permeability ranges from 10^{-9} to $10^{-10} m/s$. In the following paragraph, the numerical analyses were repeated by fixing a hydraulic permeability of $10^{-10} m/s$. As previously mentioned this value can be considered a lower bound for the measured hydraulic conductivity in the laboratory. It is worth mentioning that the previous isotropic consolidation up to 35 kPa of mean effective stress was not modelled in the numerical analyses which may have contributed in generating non-uniform void ratio distribution within the sample before shearing.

The parameters used in the series from Section 5.5.2 remain the same, except for the permeability which is decreased to $k = 10^{-10} m/s$. The aim of this series of analyses was to adequately capture the final part of the stress path, as it was assumed that the observed deviation comes from the underprediction of pore water pressures at high strain levels.

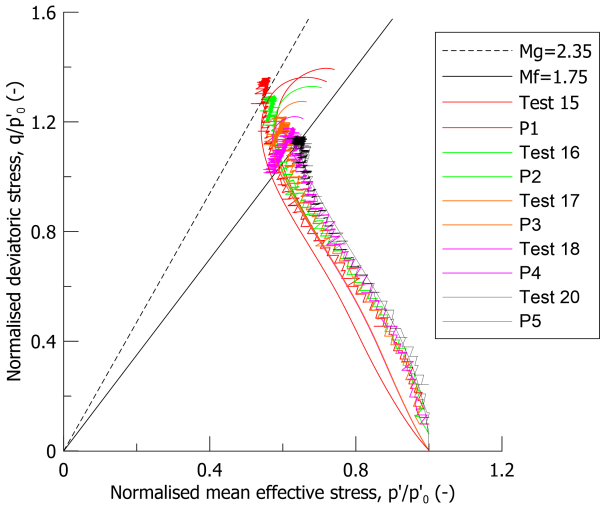

(a) Normalised effective stress path

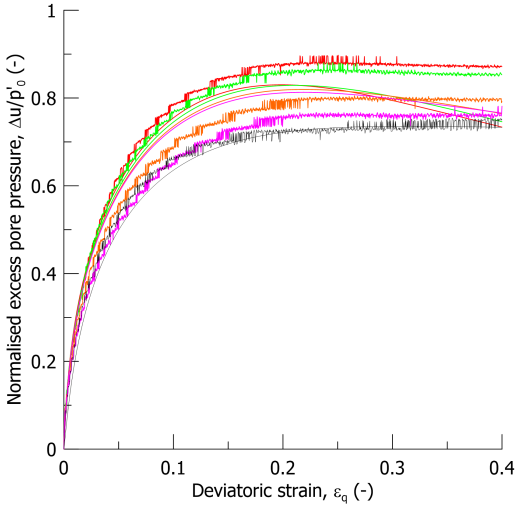

(b) Normalised excess pore pressure vs deviatoric strain

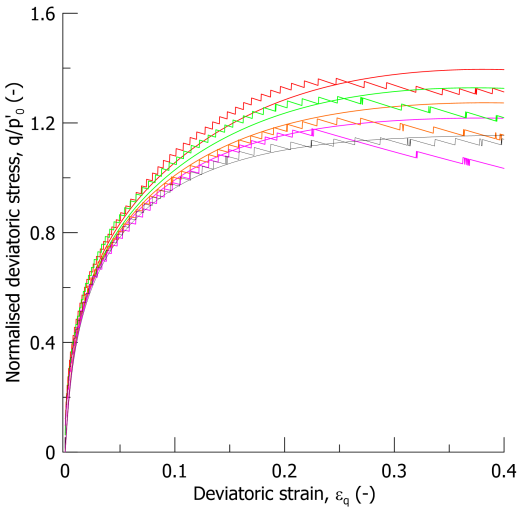

(c) Normalised deviatoric stress-strain

Figure 5.17: Results with lower permeability

Herein, for the P1 and P2 tests there is better agreement in these strain levels, while for the taller tests the pore pressures are overpredicted, as the confining pressure induced by the dead zone formation is less significant. Hence, by taking into account the softening behavior too, the final part of stress path is better captured in overall. However, due to the lower permeability from the beginning of the analysis, the initial pore water pressure build up is slightly overpredicted and the stress path, as a result, is shifted to the left and the initial convergence with the experimental results is lost.

Furthermore, the pore pressure at free failure zone for the rough tests is found to be equal to the pore pressures of Test 20, which is a smooth test. In the smooth test, it is considered that the true material behavior is observed. Thus, in the middle part, where the effect of the boundaries is minimized, the behavior is expected to be closer to the true material behavior. This can be observed, for instance, in Figure 5.18, where for the P1 Test the pore pressure measurement at mid is in a good agreement with the pore pressures from Test 20. The difference between top and mid are small like 3 kPa, but the effects at such a low effective confining stress used in peat tests in the lab are reflected in large overestimation in the mobilized friction angle if the pore pressure at the bottom is used.

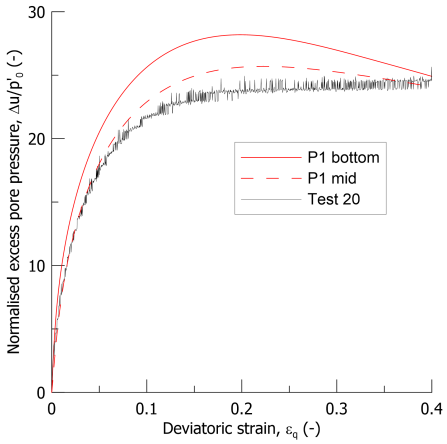

Figure 5.18: Measurements of pore pressures at bottom and mid for Test P1

Necked deformation mode

For short specimens tested with rough end platens, the deformed shape suggest a big constraint at the extremities of the sample and the lateral expansion was mainly localized in the central portion. By comparing the deformed geometries in Figure 5.19a it is observed that the results of end restraints are not captured from the adopted FEM. Contributing factor to this can also be the restraint offered by the assemblage of membrane and O-ring which is not modelled in the Thesis. This can be roughly modelled by constraining the lateral movement of some nodes at the right boundary of the mesh (Figure 5.19a) while the input parameters of the analyses are kept constant as in Section 5.5.2.

In order to better approximate the deformed shape from the experimental tests, constraining the lateral displacement of nodes relating with 3 mm at the bottom and top of the right boundary of the specimen is done. Through this way, lateral expansion of the sample at the top and bottom is prevented replicating what observed in the laboratory test (see 5.19). Consequently, the specimen is under higher confining pressure having as a result an increase in the pore pressures and the softening of pore pressures to be reduced. The results of these analyses can be depicted in Figure 5.20 where the same comments with the analyses of lower permeability can be attributed to the development of pore pressures and its consequences to the stress path. Similarly, the deviatoric stress is not influenced by this alternation.

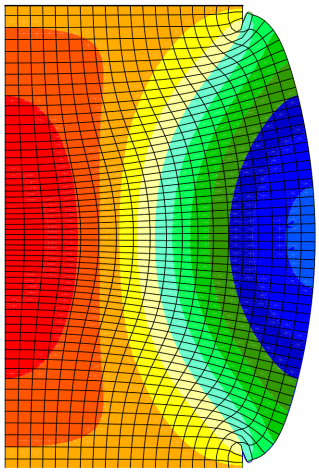

(a) Deformed mesh of Test P1 with lateral constrained nodes

(b) Deformed sample at the laboratory

Figure 5.19: Test 15

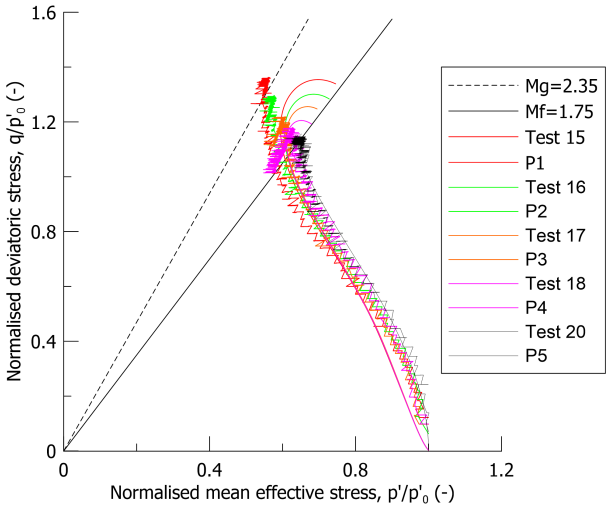

(a) Normalised effective stress path

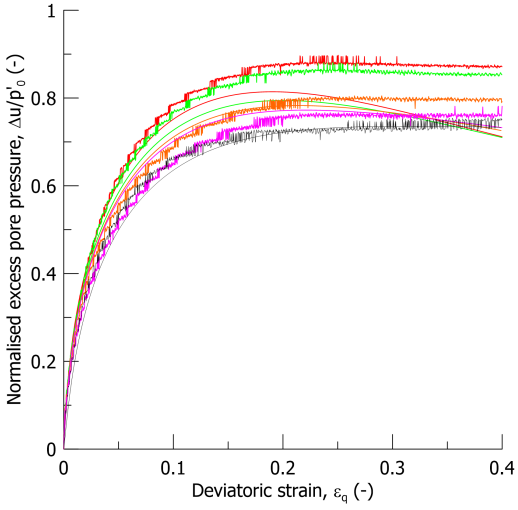

(b) Normalised excess pore pressure vs deviatoric strain

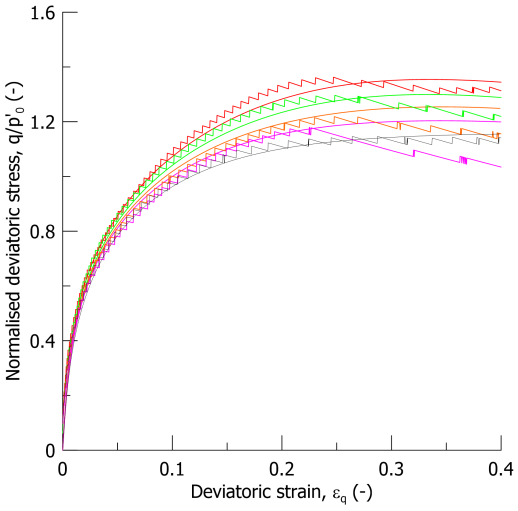

(c) Normalised deviatoric stress-strain

Figure 5.20: Results with horizontal constraints

Until now, the developed constitutive model gives reasonable results with respect to the experimental observations of the tested peat. However, it is well known that the peat formations have a large amount of fibers. The proposed constitutive model can only be used for predicting the behavior of the matrix of the peat. Hence, some deviations between the experimental and numerical results can be attributed to this. More specifically, the fibers constraint the lateral expansion of the soil and thus affect both the excess pore pressure and the deviatoric stress. This reduction of lateral expansion may lead to decreasing the softening of the pore pressures in the numerical predictions if the fibers were included in the constitutive model.

The experimental results suggest the presence of a scale effect when the sample height is increased. However, the numerical results were not able to capture this scale effect. Possible numerical approach as second gradient may be suitable to introduce a characteristic length in the problem. Again the small fibers network present in the tested peat may define the characteristic length.

5.6 TxCD tests

Herein, the proposed model is tested against TxCD tests. The available experimental tests are 3, all with rough boundaries and height to diameter ratio H/D equal to 2. The 3 tests examine the response of the fibrous peat in various stress paths, p' and η constant and unloading/reloading. In these stress control drained tests, the soil material has a preconsolidation pressure around $p'_c = 35$ kPa. A difference between the TxCU and TxCD tests lies in the flow rule used in this series, as the k_g is equal to 0.98, the value obtained by the analyses in Chapter 3. Another difference between the drained and undrained tests is the different valued of D_1, which after some preliminary calibrating analyses on Test T4, it is decided to be equal to 30. All the other parameters have been kept the same. Table 5.4 summarizes the input parameters of these FEM analyses. Finally, the numerical analyses did not account for the development of excess pore pressure assuming the tests being perfectly drained (purely mechanical analyses).

Table 5.4: Parameters of tested material for drained analyses

Numerical Test	$\boldsymbol{\lambda}$	$\boldsymbol{\kappa}$	$\boldsymbol{\nu'}$	$\boldsymbol{M_f}$	$\boldsymbol{k_f}$	$\boldsymbol{M_g}$	$\boldsymbol{k_g}$	$\boldsymbol{D_0}$	$\boldsymbol{D_1}$	$\boldsymbol{p'_0}$	$\boldsymbol{e_0}$
N4	2	0.3	0.2	1.5	3	1.75	0.98	1.2	30	32	7
N6	2	0.3	0.2	1.5	3	1.75	0.98	1.2	30	32	7.8
N34	2	0.3	0.2	1.5	3	1.75	0.98	1.2	30	38	8

Regarding the stress controlled tests, an initial constant p' stress path until the intersection of the yield surface is performed in Test T4, followed up by a constant η, and finally a constant p' stress path which goes above the critical state line due to the end restraint formation enhancing the strength of the sample. In the Test T6, there is an intermediate unloading and reloading stress path before the final constant p' stress path. Finally, for the Test T34, a constant p' path is followed up by a radial stress path along K_0-line.

In Figure 5.21a, the stress paths of the numerical and experimental tests are depicted along with their initial yield surface. It is seen that the numerical predictions of the stress paths are in a good agreement until they reach the Critical State Line. After this point, the code fails to predict the post-failure stresses. The use of a mixed volumetric and distortional hardening allows the numerical stress path to reach to higher stress ratios than the one in critical state but still well below the experimental ones.

The numerical results for the case of Test 34 are in a good qualitative and quantitative agreement with the experimental results for both the volumetric and deviatoric response (Figures 5.21b,

5.21c and 5.21d). On the other hand, the qualitative response remains good for Tests 4 and 6, but this cannot be said for the quantitative response especially for the deviatoric part of the mechanical behavior. The numerical results are not able to capture the observed response with deviatoric stress overpassing the critical state line and a softer behavior is predicted.

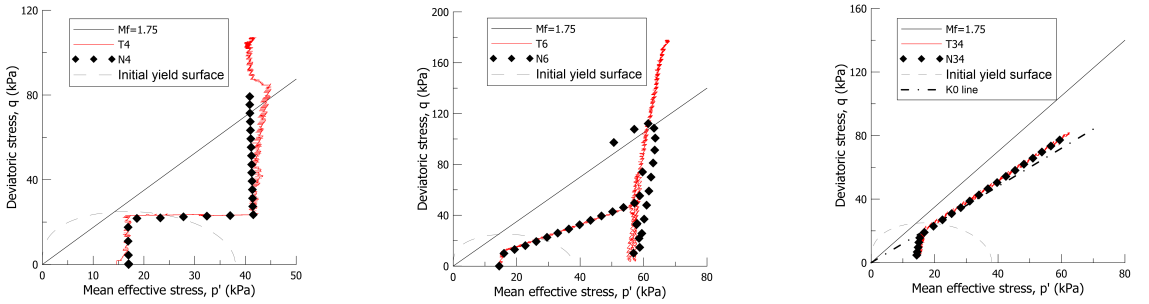

(a) Stress path

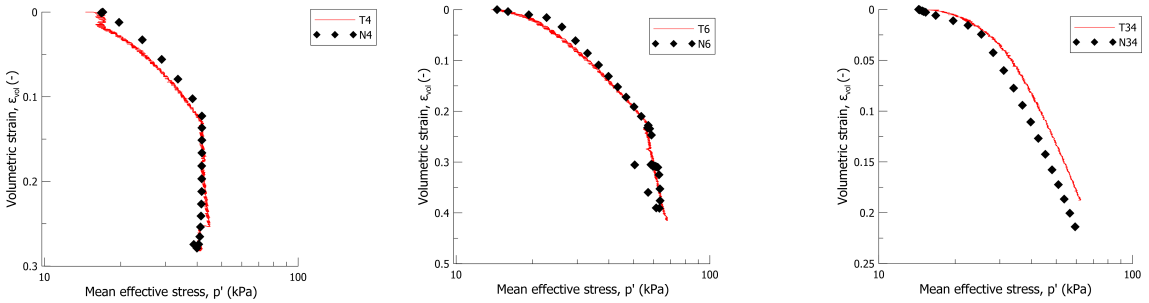

(b) Volumetric strain ε_v versus mean effective stress p'

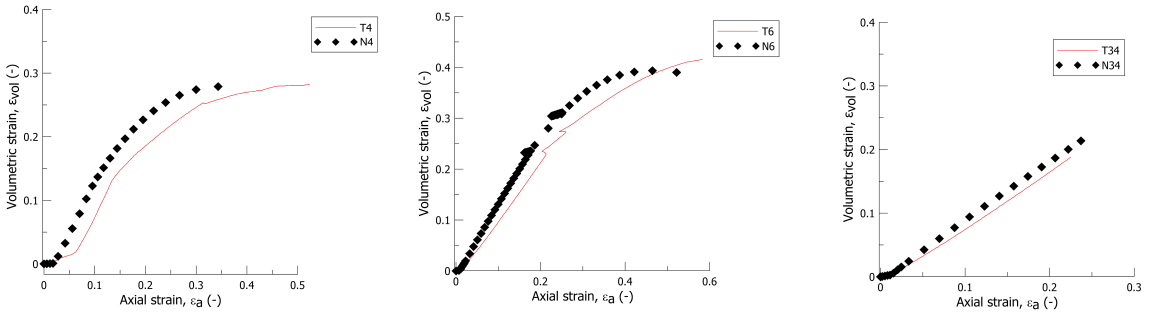

(c) Volumetric strain ε_v versus axial strain ε_a

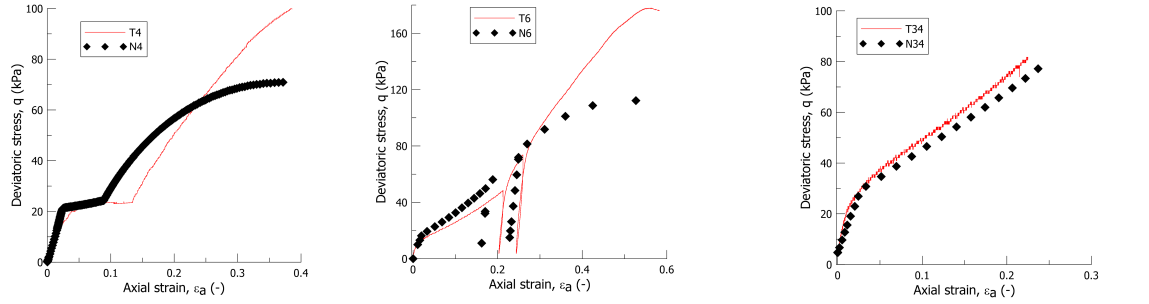

(d) Deviatoric stress q versus axial strain ε_a

Figure 5.21: Plots for Tests T4 (left), T6 (center) and T34 (right)

Discussion

To better understand the capabilities and limitations of the proposed model outlined during a TxCD test, it is useful to look into the Test T4. In Figure 5.22, the contour plots of axial strain at different strain levels for the specimen T4 are presented. With respect to end restraint phenomenon, it is clearly seen that wedges start to be formed from axial strain $\varepsilon_a = 1\%$. The wedges are fully developed at failure (Figure 5.22d), where bulging at the outer part of the specimen is observed, whereas the central part is of the specimen is compressed and carries the load.

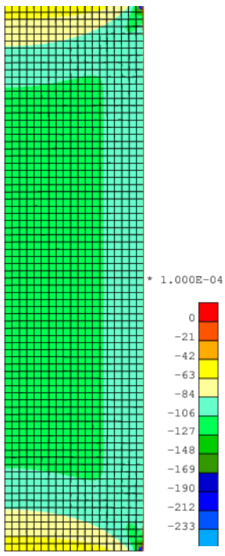

(a) $\varepsilon_a = 1\%$

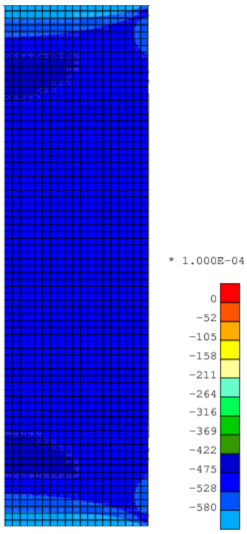

(b) $\varepsilon_a = 5\%$

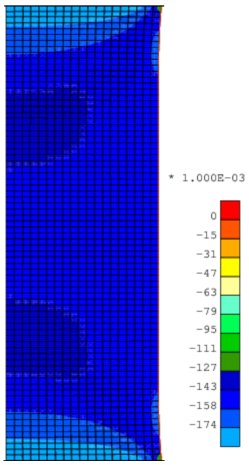

(c) $\varepsilon_a = 15\%$

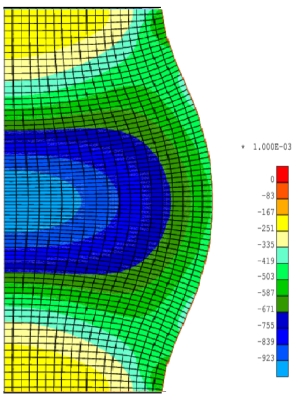

(d) $\varepsilon_a = 30\%$

Figure 5.22: Isolines of axial strain in deformed mesh at 4 different strain levels

It is worth mentioning that the behavior at the beginning is elastic, as the stress path lies inside the initial yield surface (5.21a) and a radial expansion is predicted. After the elastic radial expansion, the specimen until 15% of strain is under radial contraction and then again starts to expand and finally, the typical bulged specimen is observed. For explaining this behavior, the

dilatancy should be formulated in terms of incremental axial and radial strains:

$$d = \frac{d\varepsilon_p^p}{d\varepsilon_q^p} = \frac{d\varepsilon_a^p + 2d\varepsilon_r^p}{\frac{2}{3}(d\varepsilon_a^p - d\varepsilon_r^p)} \tag{5.16}$$

Solving in terms of incremental axial and radial strains, and expressing the dilatancy by the flow rule proposed by McDowell and Hau (2004), the ratio of incremental axial strains over radial strains yields

$$\frac{d\varepsilon_a^p}{d\varepsilon_r^p} = -\frac{2d+6}{3-2d} \tag{5.17}$$

where $d = \dfrac{M_g^2 - \eta^2}{0.98\eta}$

The 4 snapshots of the deformed mesh of the specimen are shown with bullets in Figure 5.23. In order to explain the deformation mode of the specimen, it should be taken into account that the strain simply follows the stress dilatancy rule in the sense that the flow rule prescribes the link between the stress ratio and the plastic strain. By Eq. (5.17),the amount of contraction or expansion is given by the dilatancy. More specifically, the deviatoric stress increases in Test T4 with the axial strain but the stress ratio does not follow a monotonic response due to the different stress path followed. Thus, by linking the stress ratio with the ratio of plastic axial strains to radial strains in Figure 5.23c, the theoretical curve and the predicted by the code with global stress-strain elaboration is presented. The first point on Figure 5.23c is not relevant because the behavior is elastic. For stress ratio $\eta < \eta_{K_0}$ the axial and radial component of strain have the same sign, meaning that axial and radial contraction takes place. For larger stress ratios, the sign of the ratio is reversed and radial expansion occurs.

The above can be used in order to evaluate the deformational behavior of the specimen in Figure 5.23d. Initially, the behavior is elastic so the prescribed deformational behavior by the flow rule does not apply and consequently, there is expansion. After the yielding of the material, the flow rule prescribes a contractive behavior until 15% of axial strain. At this point, the stress ratio is close to η_{K_0} and the flow rule dictates radial expansion to take place for larger η. At this point, in Figure 5.23d a flex point is observed and the sample starts to expand radially until failure.

In addition, Figure 5.23d depicts the experimental development of axial strain versus radial strain too. The code captures the following trends in the strain response. However, as it has been already mentioned, one major limitation of the proposed model is its inadequacy to reach to higher deviatoric stresses after reaching the Critical State Line. An explanation to this is the prediction of excessive displacements by the numerical code (Figure 5.23d), which can be attributed to the exclusion of fibers from the constitutive model. In the same way with the undrained tests, where the volumetric part of the behavior (pore pressures) was not captured well after a strain level, the possible explanation to this limitation in drained tests is that the fibers in reality start to contribute to the deformation mode of the sample by stretching and restraining the lateral expansion. This leads to the development of higher deviatoric stresses and lower axial and radial strains in contrast to the model predictions. Finally, it can be seen that the elastic contribution to the total deformation of the sample in the laboratory is bigger than in the numerical code. This is related to the implemented elastic law, because in peat it is difficult to define the elastic domain as plastic strains are generated from the start of stress path.

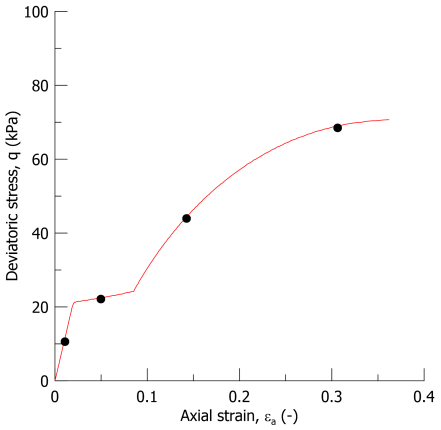

(a) Deviatoric stress q versus axial strain ε_a

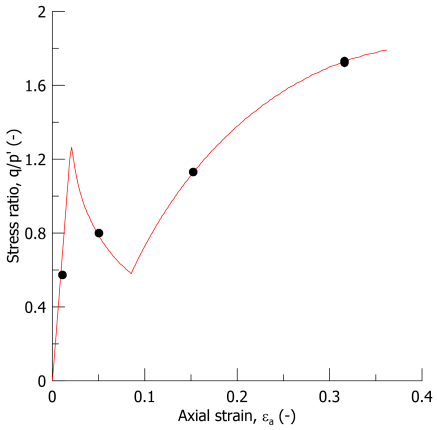

(b) Stress ratio η versus axial strain ε_a

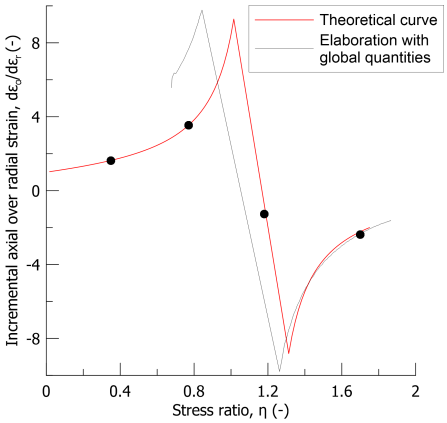

(c) Incremental ratio of plastic axial to radial strains versus stress ratio

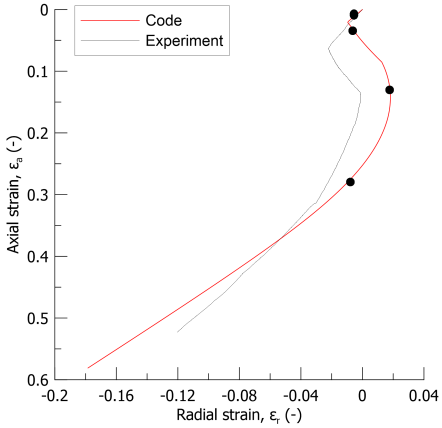

(d) Axial strain versus radial strain

Figure 5.23: Test T4

Another issue discussed here is that different flow rules for drained and undrained tests are used. In order to investigate this limitation of the proposed constitutive model, it is worth to focus on Figure 5.24, where the radial-axial strain paths are plotted for peat tests under isochoric, K_0 paths and isotropic compression paths. A distinction should be made between strain paths corresponding to lateral expansion (fibres stretching) and lateral contraction (fibres entanglement). The latter situation is depicted on the top right quadrant, where the fibres-matrix interaction is limited. Namely, during isotropic compression path, the fibres are not stretched due to compressive radial strains and the mechanical response is not enhanced by the fibers tensioning. In K_0 path ($\varepsilon_r = 0$), where the effect of fibres is substantially switched off, the fibres flattening in the vertical direction but with no stretching is promoted (Muraro, 2018).

On the contrary, the stretching of the fibers due to radial expansion of specimens results to increased fibres-matrix interaction. With the progressive radial expansion of the sample, the frictional interaction between the soil matrix and the fibrous network is promoted with consequent evolution of the peat fabric and alteration of the plastic deformational response. Isochoric test, as the undrained compression tests, on sample 5 is expected to magnify the most this interaction. More specifically, under isochoric conditions, it is required the axial compression to be compensated by the radial expansion. Under drained conditions there is no such a kinematic constraint. Hence, the radial strains under undrained conditions are larger than under drained conditions given the same amount of axial strain.

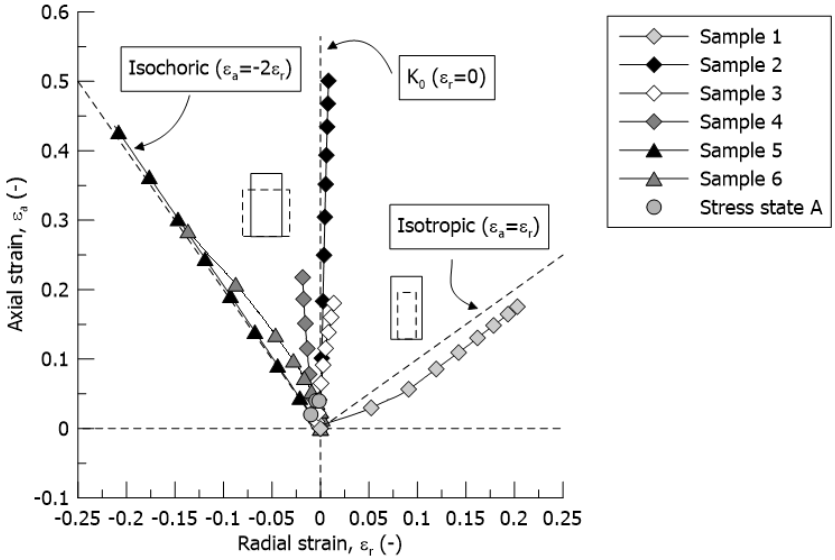

Figure 5.24: Radial-axial strains paths for peat samples (adopted by Muraro, 2018)

This alternation of the plastic deformational response is due to the induced anisotropy taking place by the different amount of stretching of the fibers resulting by the radial strains of the specimens. According to Diambra et al. (2013), for the case of general fibers-reinforced soils, as well as for peats, radial strains rather than deviatoric strains seem to rule the matrix-fibres interaction. The matrix-fibers interaction and the induced anisotropy due to different strain paths is taken into account by changing the flow rule of the model. This limitation of the model, thus, is associated with the non inclusion of the peat fabric, consisting of fibers, in the formulation of the constitutive model. For the case of flow rule used in undrained simulations, the flow rule dictates that the radial strains should be expansive from small stress ratio in contrast to the flow rule of drained tests (Figure 5.25b). This is also observed in the shapes of plastic potentials (Figure 5.25a), where the plastic potential for the ($k_g = 15$) has a tear type magnifying the relevance of the distortional strains on the plastic deformation mechanism and for the ($k_g = 0.98$) a bullet shape with plastic strains increment vectors mainly ruled by volumetric strains. Note that expansive radial strains mean higher deviatoric strains, and the plastic strain increment consequently must be inclined towards the q axis.

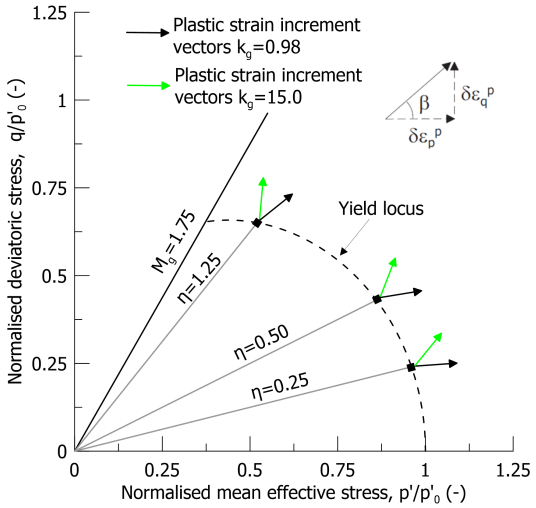

(a) Plastic strain vectors for different radial stress paths

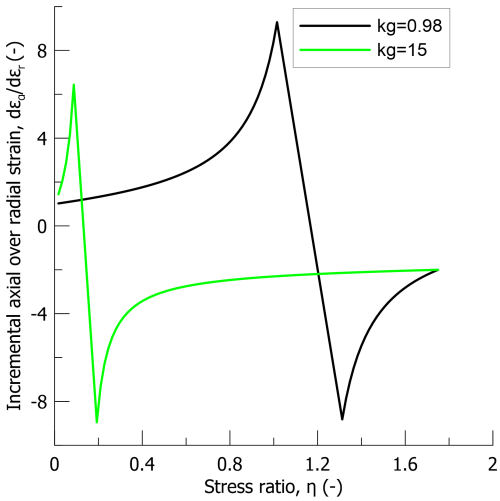

(b) Incremental ratio of plastic axial to radial strains versus stress ratio

Figure 5.25: The two different flow rules used in the model

5.7 Conclusions

In summary, in this chapter the constitutive model was implemented into the FEM programme LAGAMINE. The proposed model has in total 10 parameters. The determination of the vast majority of the parameters is based on well known procedures, already used for calibrating model parameters, as they are based on MCc model and only six additional parameters are introduced. 4 out of 6 additional parameters provide a flexibility on the selection range of yield surfaces and plastic potentials. It is possible to choose between tear type or bullet type shapes. In addition, the two remaining parameters control the amount of contribution of plastic deviatoric strains in the hardening law.

The model was tested against experimental evidences in both drained and undrained compression conditions under the influence of the end restraints. For the latter case, the response until the critical state is well captured by the model. In more detail, the non homogeneous field of excess pore pressure due to end restraints was successfully captured. In addition, measures of the pore pressure at the mid height of the sample are important, where the effect of the boundaries is minimised and the behavior is expected to be more representative to the true material behavior. However, the increased deviatoric stresses due to end restraints were not successfully captured by the model, as no difference in the deviatoric stresses at failure for different height to diameter ratios is observed. To achieve this, the hardening parameter D_1 should be adjusted to the geometry of the sample. Thus, from a modelling point of view, the distortional hardening seems to be linked with the geometry effects due to internal length effects by the presence of peat fibers. Moreover, the lack of fibers from the constitutive model results also to an increased lateral expansion of the specimens which is not observed experimentally. The fibers, in reality, during the radial expansion are stretched offering a confinement to the specimen and reducing its radial expansion. By constraining some nodes at the bottom and the top of the lateral boundary of the mesh, the effect of platens is magnified in order to roughly replicate the observed deformation mode in the laboratory. The results showed a better approximation of the experimental results. However, this approximation can be used only for rough indications

The mechanical response from drained triaxial compression tests until the critical state is well captured by the model. The model suffers at the post-critical state region as it cannot capture the high experimental deviatoric stresses despite the possibility of attaining stress ratios above critical state thanks to the introduction of the mixed volumetric and distortional hardening. The stress-strain response until the critical state is in good agreement with the experimental evidence up to strain level of 25%, but excessive deformations are predicted in the post-critical state region due to the non inclusion of fibers in the constitutive relationships which provide a reinforcement to the radial expansion.

Due to the non inclusion of fibers in the constitutive model and the resulting deficient description of matrix-fiber interaction, the radial expansion cannot be restrained and the different kinematic mechanisms developing in undrained and drained tests cannot be described by using the same parameters in each case. For drained tests, there is a volumetric response, and the plastic potential should have a tear type. For the undrained tests, there is no volumetric strain and consequently, radial expansion should compensate for the axial compression. Due to this, the deviatoric strains become more significant and a bullet type plastic potential is more suitable. The limitation of using two different plastic potentials for simulating isochoric and non-isochoric strain fields comes from the induced anisotropy of the peat fabric due to the matrix-fibers interactions and its lack of contribution to the mechanical behavior. One way of dealing with it is to introduce a hardening parameter of the plastic potential, which tracks the stretching of the fibers and consequently changes the shape of the plastic potential.

Chapter 6

Summary and Discussion

The modelling of the deviatoric behavior of peat is of primary importance for many applications of geotechnical engineering. Peat is well known for ensuing a plethora of construction challenges on dykes and embankments. In contrast to the modelling of the volumetric behavior of peat where there are many remarkable attempts, the proposed models for the deviatoric counterpart are rather scarce.

The main objective of this Thesis is to investigate numerically the deviatoric behavior of peat, and to propose a modelling framework which will be able to capture the behavior of peat. After an extensive literature review on the well established MCc model and on the various research concerning ways of dealing with the limitations of this model, a model for understanding and modelling quite adequately the mechanical response of peat has been proposed.

6.1 Conclusions

The conclusions of this Thesis are presented with reference to the research questions posed in Chapter 1.

Is associated plasticity suitable for describing the pre-failure behavior of peat specimens affected by end restraints? Which method of measuring global stresses and strains is more suitable for describing the pre-failure stress-strain response of peat?

Experimental results along K_0 line allow to define the shape of the plastic potential for the tested peat, using the flow rule proposed by McDowell and Hau (2004). This shape differs from the plastic potential surface of MCc model due to the well known limitation of MCc on predicting correctly the K_0 value.

End restraints affect the derivation of the stress dilatancy rule. Traditionally, the $d - \eta$ rule, derived from tests with rough ends by elaborating the results with global measurements, is different than the material flow rule. Below K_0 the dilatancy is below the material flow rule, while the opposite is observed for radial paths above K_0.

FEM analyses were run to replicate the experimental results with rough end platens. More suitable global measurement is the use of the average diameter between the nominal diameter of the cap and the equivalent cylinder diameter. Using the flow rule predicting correctly the K_0 value, the predictions are in good agreement for radial paths below K_0. On contrary, for radial paths above K_0, higher dilatancy is observed experimentally than in the numerical simulation,

and the necessity, from a modelling point of view, of adding the deviatoric hardening in the constitutive model is, afterwards, highlighted.

Why the yield surface introduced by the Modified Cam clay model (Roscoe and Burland, 1968) is inappropriate to describe the peat behavior and how the formulation of the yield surface should be modified in order to have satisfying results?

By integrating the non-associated flow rule proposed by McDowell and Hau (2004) generalized shapes of plastic potential surfaces can be retrieved. These plastic potential surfaces can be adopted and be used as yield surfaces, offering flexibility on the shapes of the yield surfaces. By calibrating the parameters, a yield surface representative to the material under investigation can be generated, as for the tested peat the yield points form a different yield locus than the employed yield surface of MCc, which is slightly above the experimentally observed one.

Is the hardening law used in the majority of constitutive models based on Cam clay theory appropriate for capturing the stress strain behavior of peat? If not, how can this be tackled?

Based on the literature, the addition of deviatoric hardening in the hardening law of Cam clay theory results to higher dilatancy and higher stresses obliquity. In addition, the "hook" in the undrained stress paths of the peat specimens can be modelled through this way.

An extension of MCc has been incorporated by assuming that deviatoric plastic strains also contribute to hardening. Two parameters are introduced D_0 and D_1. By setting $D_0 = 0$, the MCc model is retrieved. It has been found that the deviatoric contribution to the soil hardening change profoundly the performance of the new model. In particular, higher stress obliquity and continuous dilation is observed for higher values of D_0. By keeping the D_1 null, the critical state is not reached, because the size of yield surface is dependent on both the plastic volumetric and deviatoric strain increments, and the latter is not zero at critical state. By increasing the D_1, critical state is asymptotically reached.

How the model performs if the experiments are treated numerically as a Boundary Value Problem?

All the above elastoplastic ingredients were combined in a simple elastic-plastic non associative model with mixed volumetric and distortional hardening for the deviatoric behaviour of peat. The model has in total 10 parameters with a relatively easy way of determining them. These are the slope of the isotropic normal compression line λ, the slope of the isotropic unloading and reloading line κ, the Poisson's ratio ν', the initial void ratio e, the M_f, M_g, k_f, k_g and the hardening parameters D_0 and D_1.

In an attempt to overcome end restraint effects on both the shear strength and deformation mode of peat, the model has been formulated in the multi-axial stress space and implemented in the Finite Element code LAGAMINE. The experimental tests were then simulated as boundary values problems for both TxCU and TxCD tests.

For the former case, the response until the critical state is well captured by the model. In more detail, the non homogeneous field of excess pore pressure due to end restraints was successfully captured. In addition, measures of the pore pressure at the mid height of the sample are important, where the effect of the boundaries is minimised and the behavior is expected to be more representative to the true material behavior. However, the increased deviatoric stresses due to end restraints were not successfully captured by the model, as no difference in the

deviatoric stresses at failure for different height to diameter ratios is observed. To achieve this, the hardening parameter D_1 should be adjusted to the geometry of the sample. Thus, from a modelling point of view, the distortional hardening seems to be linked with the geometry effects due to internal length effects by the presence of peat fibers. Moreover, the lack of fibers from the constitutive model results also to an increased dilation of the specimens which is not observed experimentally. The fibers, in reality, during the radial expansion are stretched offering a confinement to the specimen and reducing its radial expansion. By constraining some nodes at the bottom and the top of the lateral boundary of the mesh, the effect of platens is magnified in order to roughly replicate the observed deformation mode in the laboratory. The results showed a better approximation of the experimental results. However, this approximation can be used only for rough indications

The mechanical response from drained triaxial compression tests until the critical state is well captured by the model. The model suffers at the post-critical state region as it cannot capture the high experimental deviatoric stresses despite the possibility of attaining stress ratios above critical state thanks to the introduction of the mixed volumetric and distortional hardening. The strain response until the critical state is in good agreement with the experimental evidence up to strain level of 25%, but excessive deformations are predicted in the post-critical state region due to the non inclusion of fibers in the constitutive relationships which provide a reinforcement to the radial expansion. More specifically, the high strain level above 25% attained in the drained tests magnify the matrix-fiber interaction and the additional stretching of the fibers for strains above 25% cannot be neglected anymore.

Due to the non inclusion of fibers in the constitutive model, the radial expansion cannot be restrained and the different kinematic mechanisms developing in undrained and drained tests cannot be described by using the same parameters in each case. For drained tests, there is a volumetric response, and the plastic potential should have a bullet type. For the undrained tests, there is no volumetric strain and consequently, radial expansion should compensate for the axial compression. Due to this, the deviatoric strains become more significant and a tear type plastic potential is more suitable. The limitation of using two different plastic potentials for simulating isochoric and non-isochoric strain fields comes from the induced anisotropy of the peat fabric due to the matrix-fibers interaction and its lack of contribution to the mechanical behavior. One way of dealing with it is to introduce a hardening parameter of the plastic potential, which tracks the stretching of the fibers and consequently changes the shape of the plastic potential.

6.2 Recommendations

The recommendations of this Thesis for future research will be focused on the limitations outlined in the conclusions and the general limitations discussed in the Chapter 1.

For managing to capture the high deviatoric stresses developing in the experiments, but also reducing the radial expansion in the numerical simulations, the fibers should be included in the formulation of the constitutive model by means of fabric tensor. There are a lot of studies on reinforced soils, where the underlying theory can be studied.

It is well known that the peat is an extremely anisotropic material. However, in this study the peat behavior is modelled by isotropic yield surfaces and plastic potentials surfaces, implementation which poses some limitations at the deformation mechanism between isochoric and non-isochoric deformational modes. It seems that the plastic strain vector under these two deformational modes is ruled by the amount of stretching of the fibers leading to a nonholonomic response. The contribution of the fibers in the deformational mode under different stress paths

is, thus, related to the induced anisotropy coming from the stretching of the fibers. A solution to this limitations would be a hardening parameter, which would track the stretching of the fibers, and accordingly to change the plastic potential shape.

Based on the limitations outlined in the Chapter 1, creep strains development is a major aspect of the soft soils like peat and it would be useful this phenomenon to be modelled by means of visco-plasticity. Moreover, in partially saturated peats, gas bubbles are developed during triaxial tests. This feature could be modelled by a Thermo-Hydro-Gas-Mechanical coupled analysis. In addition, in this study an axisymmetric 2D analyses have been employed, despite the fact that the observed behavior in the laboratory indicates that a 3D analysis would be more accurate.

Finally, despite the outlined limitations of the model, it would be useful to test its performance on a field application. The model is capable of describing the peat behavior until 20% of strain under triaxial testing, strain level which barely is exceeded on field. Hence, the performance of the model could be evaluated on real field applications and necessary results for its development to be retrieved.

Bibliography

Alonso, E. E., Gens, A., and Josa, A. (1990). A constitutive model for partially saturated soils. *Géotechnique*, 40(3):405–430.

Atkinson, J. H. and Bransby, P. L. (1977). *The mechanics of soils : an introduction to critical state soil mechanics*. University series in civil engineering. McGraw-Hill, London.

Bishop, A. W. and Green, G. E. (1965). The influence of end restraint on the compression strength of a cohesionless soil. *Géotechnique*, 15(3):243–266.

Borja, R. I. and Kavazanjian, E. J. (1985). A constitutive model for the stress-strain-time behaviour of wet clays. *Géotechnique*, 35(3):283–298.

Chandler, H. W. (1990). Homogeneous and localised deformation in granular materials: A mechanistic model. *International Journal of Engineering Science*, 28(8):719–734.

den Haan, E. (2014). Modelling peat with an anisotropic time-dependent model for clay. *Numerical Methods in Geotechnical Engineering*, page 55.

den Haan, E. and Feddema, A. (2013). Deformation and strength of embankments on soft dutch soil. *Proceedings of the Institution of Civil Engineers - Geotechnical Engineering*, 166(3):239–252.

Diambra, A., Ibraim, E., Russell, A. R., and Muir Wood, D. (2013). Fibre reinforced sands: from experiments to modelling and beyond. *International Journal for Numerical and Analytical Methods in Geomechanics*, 37(15):2427–2455.

Dieudonné, A.-C. (2016). *Hydromechanical behaviour of compacted bentonite: from micro-scale analysis to macro-scale modelling*. Doctoral dissertation, Université de Liège, Liège, Belgique.

Drucker, D. (1959). A definition of stable inelastic material. *Jour. of App. Mech.*, 26:101–106.

Drucker, D. C. and Prager, W. (1952). Soil mechanics and plastic analysis or limit design. *Quaterly of Applied Mathematics*, 10(2):157–165.

Farrell, E., Jonker, S., Knibbeler, A., and Brinkgreve, R. (1999). The use of direct simple shear test for the design of a motorway on peat l'utilisation du test de cisaillement simple direct pour la conception d'une autoroute sur tourbe. In *Geotechnical Engineering for Transportation Infrastructure: Theory and Practice, Planning and Design, Construction and Maintenance: Proceedings of the Twelfth European Conference on Soil Mechanics and Geotechnical Engineering, Amsterdam, Netherlands, 7-10 June 1999*, volume 2, page 1027. CRC Press.

Gens, A. (1982). A theoretical model for describing the behavior of soil not obeying rendulic's principle. In *Int. Symp. on Numerical Models in Geomechanics*. Balkema (ed.).

Gens, A. and Potts, D. M. (1988). Critical state models in computational geomechanics. *Engineering Computations*, 5(3):178–197.

Lade, P. and Tsai, J. (1985). Effects of localization in triaxial tests on clay. proceedings of the eleventh international conference on soil mechanics and foundation engineering, San Francisco, 12-16 august 1985. *Publication of: Balkema (AA)*.

Lagioia, R. and Panteghini, A. (2014). The influence of the plastic potential on plane strain failure. *International Journal for Numerical and Analytical Methods in Geomechanics*, 38(8):844–862.

Lagioia, R., Puzrin, A. M., and Potts, D. M. (1996). A new versatile expression for yield and plastic potential surfaces. *Computers and Geotechnics*, 19(3):171–191.

Landva, A. and La Rochelle, P. (1983). Compressibility and shear characteristics of radforth peats. In *Testing of peats and organic soils*. ASTM International.

Li, X. S. and Dafalias, Y. F. (2000). Dilatancy for cohesionless soils. *Géotechnique*, 50(4):449–460.

Matsuoka, H. and Nakai, T. (1974). Stress-deformation and strength characteristics of soil under three different principal stresses. In *Proceedings of the Japan Society of Civil Engineers*, volume 1974, pages 59–70. Japan Society of Civil Engineers.

McDowell, G. R. and Hau, K. W. (2004). A generalised Modified Cam clay model for clay and sand incorporating kinematic hardening and bounding surface plasticity. *Granular Matter*, 6(1):11–16.

Mesri, G. and Ajlouni, M. (2007). Engineering Properties of Fibrous Peats. *Journal of Geotechnical and Geoenvironmental Engineering*, 133(7):850–866.

Muir Wood, D. (1990). *Soil Behaviour and Critical State Soil Mechanics*. Cambridge university press.

Muraro, S. (2018). *PhD Thesis on the Mechanical behavior of peat*. Phd dissertation, Delft University of Technology.

Muraro, S. and Jommi, C. (2018). Implication of end restraint in triaxial tests on the derivation of the stress-dilatancy rule for soils having high compressibility. *Canadian Geotechnical Journal*, (ja).

Nova, R. (1977). On the hardening of soils. *Archives of Mechanics*, 29(3):445–458.

Nova, R. and Wood, D. M. (1978). Experimental programme to define the yield function for sand. *Soils and Foundations*, 18(4):77–86.

Nova, R. and Wood, D. M. (1979). A constitutive model for sand in triaxial compression. *International Journal for Numerical and Analytical Methods in Geomechanics*, 3(3):255–278.

Ohmaki, S. (1982). Stress-strain behaviour of anisotropically, normally consolidated cohesive soil. In *Proc. 1st Int. Symp. Num. Mod. Geomech., Zurich, 25&*, volume 269.

Ohta, H. and Wroth, C. (1976). Anisotropy and stress reorientation in clay under load. In *Proceeding of 2nd international conference on numerical methods in geomechanics, Blacksburg*, volume 1, pages 319–328.

Onaka, S. (2012). Comment on "a comparison of the von Mises and Hencky equivalent strains for use in simple shear experiments". *Philosophical Magazine*, 92(18):2264–2271.

Ortiz, M. and Simo, J. C. (1986). An analysis of a new class of integration algorithms for elasto-plastic constitutive relations. *International Journal for Numerical Methods in Engineering*, 23(3):353–366.

Praastrup, U., Jakobsen, K. P., and Ibsen, L. B. (1999). Two theoretically consistent methods for analysing triaxial tests. *Computers and Geotechnics*, 25(3):157 – 170.

Radforth, N. (1969). Muskeg as an engineering problem. Muskeg engineering handbook, 3-30.

Roscoe, K. H. and Burland, J. (1968). *On the Generalized Stress-Strain Behavior of Wet Clays*.

Roscoe, K. H., Schofield, A. N., and Thurairajah, A. (1963). Yielding of clays in states wetter than critical. *Géotechnique*, 13(3):211–240.

Roscoe, K. H., Schofield, A. N., and Wroth, C. P. (1958). On the yielding of soils. *Géotechnique*, 8(1):22–53.

Rowe, P. and Barden, L. (1964). Importance of free ends in triaxial testing. *Journal of Soil Mechanics & Foundations Div*, 90(Proc. Paper 3753).

Rowe, P. W. (1962). The stress-dilatancy relation for static equilibrium of an assembly of particles in contact. *Proceedings of the Royal Society of London. Series A, Mathematical and Physical Sciences*, 269(1339):500–527.

Schofield, A. and Wroth, P. (1968). *Critical state soil mechanics*, volume 310. McGraw-Hill London.

Sheng, D., Sloan, S. W., and Yu, H. S. (2000). Aspects of finite element implementation of critical state models. *Computational Mechanics*, 26(2):185–196.

Sheng, D., Westerberg, B., Mattsson, H., and Axelsson, K. (1997). Effects of end restraint and strain rate in triaxial tests. *Computers and Geotechnics*, 21(3):163–182.

Shockley, W. G. and Ahlvin, R. G. (1960). Nonuniform conditions in triaxial test specimens. In *Research conference on shear strength of cohesive soils*, pages 341–357. ASCE.

Sloan, S. W., Abbo, A. J., and Sheng, D. (2001). Refined explicit integration of elastoplastic models with automatic error control. *Engineering Computations*, 18(1/2):121–194.

Taylor, D. (1941). 7th progress report on shear strength to us engineers. *Massachusetts Institute of Technology*.

van der Heijden, E., Bouman, F., and Boon, J. J. (1994). Anatomy of recent and peatified Calluna vulgaris stems: implications for coal maceral formation. *International Journal of Coal Geology*, 25(1):1–25.

van Eekelen, H. A. (1980). Isotropic yield surfaces in three dimensions for use in soil mechanics. *International Journal for Numerical and Analytical Methods in Geomechanics*, 4(1):89–101.

Whittle, A. J. (1993). Evaluation of a constitutive model for overconsolidated clays. *Géotechnique*, 43(2):289–313.

Wilde, P. (1977). Two invariants-dependent models of granular media. *Archives of Mechanics*, 26(6):799–809.

Yamaguchi, H., Ohira, Y., Kogure, K., and Mori, S. (1985). Undrained shear characteristics of normally consolidated peat under triaxial compression and extension conditions. *Soils and Foundations*, 25(3):1–18.

Yang, Z. X., Zhao, C. F., Xu, C. J., Wilkinson, S. P., Cai, Y. Q., and Pan, K. (2016). Modelling the engineering behaviour of fibrous peat formed due to rapid anthropogenic terrestrialization in Hangzhou, China. *Engineering Geology*, 215:25–35.

Yin, J. H. and Graham, J. (1999). Elastic viscoplastic modelling of the time-dependent stress-strain behaviour of soils. *Canadian Geotechnical Journal / Revue Canadienne de Géotechnique*, 36(4):736–745.

Yu, H. S. (1998). Casm: a unified state parameter model for clay and sand. *International Journal for Numerical and Analytical Methods in Geomechanics*, 22(8):621–653.

Zhang, L. and O'Kelly, B. C. (2014). The principle of effective stress and triaxial compression testing of peat. *Proceedings of the Institution of Civil Engineers - Geotechnical Engineering*, 167(1):40–50.